AIAA SciTech Forum
12-16 January 2026, Orlando, FL
AIAA SCITECH 2026 Forum

10.2514/6.2026-0550

Design and Piloted Simulation of Envelope-Protected Control for Flying Wing Aircraft

Direnc Atmaca*, Olaf Stroosma† and Erik-Jan van Kampen‡
Delft University of Technology, Kluyverweg 1, 2629 HS, Delft, The Netherlands

Commercial applications of flying wing aircraft present a unique opportunity to improve fuel efficiency in aviation, but also pose significant challenges in stability and control. This paper improves the existing flight control laws of a commercial flying wing concept called the Flying V. The paper designs and evaluates normal law flight controls through piloted flight simulations on a moving base flight simulator, assessing handling qualities, certification compliance, and flight envelope protection capabilities. Industry-inspired outer guidance loops include envelope protections for angle of attack, bank, pitch, and load factor, using command limiting exponential potential functions to smoothly enforce limits and prevent longitudinal instability. The inner loop employs incremental nonlinear dynamic inversion. Results demonstrate that the Flying V model, augmented with the proposed controller, achieves Level 1 handling qualities and meets nearly all certification requirements. Flight envelope protection maneuvers confirm that exponential potential functions deliver protection performance comparable to commercial aircraft and successfully prevent unstable behavior.

I. Introduction

Demand for civil aviation is projected to grow 4.3% annually over the next 20 years [§]. Although this signals a positive future for the sector, it also presents a challenge due to increasing regulations on emissions. With the global push toward carbon neutrality, the aviation sector must adopt sustainable practices to make airplanes quieter and more efficient. Most aircraft consist of a conventional tube-and-wing configuration, which has dominated the market for the last 50 years [1]. Unfortunately, despite major breakthroughs and improvements in aircraft design since the invention of airplanes, the fuel efficiency of conventional layout has been approaching an asymptote. This motivates the search for alternative configurations such as blended wing body and flying wings.

A. Flying Wings and the Flying V

In conventional aircraft, most of the lift is generated by the wings, while the fuselage holds passengers and cargo. By integrating the wings and fuselage, flying wings achieve higher lift-to-drag ratios, increasing fuel efficiency. However, although there have been several applications of flying wings for military purposes, a fully developed commercial application is yet to be realized. This is partly due to a lack of stabilizing surfaces on flying wings, which raises concerns due to strict commercial aviation requirements, and makes flight control augmentation essential for flying wing aircraft.

A promising long-range commercial flying wing concept is the FLYING V[TM¶]. Compared to the Airbus A350-1000, the Flying V is 20% more fuel-efficient with a similar size and capacity [2]. Regardless of its potential for lower emissions and fuel savings, the Flying V, like all flying wing aircraft, suffers from limited stability and control authority [3]. Recent studies indicate that the Flying V exhibits Dutch roll instability and nonlinear behaviors, such as pitch break [4, 5] and decreased control effectiveness with increasing angle of attack and sideslip [6]. To address these issues and explore the Flying V further, research and development activities continue, focusing on aerodynamics, structures, engine integration, airport operations, climate impact, noise, stability, control, and handling qualities. For a deeper investigation between Flying V and conventional aircraft configurations, the reader is referred to [2, 4–14].

From the perspective of a control engineer, incorporating flight control systems (FCS) is the most direct way to address these undesirable attributes of the Flying V, without requiring major structural changes. Flight control

Accepted for publication in the Journal of Guidance, Control, and Dynamics
*PhD Candidate, Control and Simulation, Faculty of Aerospace Engineering; d.atmaca@tudelft.nl (Corresponding author)
†Senior Researcher, Control and Simulation, Faculty of Aerospace Engineering; o.stroosma@tudelft.nl
‡Associate Professor, Control and Simulation, Faculty of Aerospace Engineering; e.vankampen@tudelft.nl
§`https://www2023.icao.int/Meetings/FutureOfAviation/Pages/default.aspx` [Accessed: May 19, 2025]
¶Flying V is a trademark of Fortescue. The Flying V design is owned by Fortescue, UK & NL patents pending.

augmentation can improve dynamic modes, optimize control surface allocation, and enforce safe flight envelope limits. Recently, two studies focused on designing such control systems [7] and analyzing their impact on handling qualities through piloted flight simulation [8]. These papers reported significant improvements in the stability of the dynamic modes and handling qualities compared to the unaugmented airframe. Some extensions of this work to fault-tolerant flight control even demonstrated flight safety under actuator faults [15]. However, flight simulations [8] also revealed several issues, such as pitch dropout, lack of pitch compensation during turns, overshoot in the response of the flight envelope protection (FEP), and some model fidelity concerns. This study aims to address these problems.

B. Fly-By-Wire Flight Control

The majority of modern airliners have three fundamental control modes: normal, alternate, and direct flight law. In direct law, pilot commands are manually mapped over the control surfaces, which means that the pilot directly controls the surfaces during flight. In normal law, a fly-by-wire (FBW) control system stands between the pilot and the control actuators. In this control mode, the pilot commands a reference motion for the aircraft. This motion is then interpreted by the flight control system, and with the help of flight computers, the necessary control deflections are calculated to follow the reference set by the pilot. The reference motion that the pilot commands depends on the flight control implementation. For instance, Airbus uses the C^* parameter for pitch control [16], while Boeing uses C^*U [17–19]. The C^* parameter combines pitch rate and load factor and is initially designed as a handling quality criterion [20]. Nowadays, it is a well-established method used in longitudinal FBW control laws. Lastly, the alternate law is similar to the normal law; however, with reduced capabilities.

An important component of a FBW controller is the flight envelope protection system. Consequently, FEP is an active research field not only for aircraft but also for a wide range of aerospace vehicles [21–25]. The goal of FEP is to restrict the aircraft to its safe operating envelope. In general, there are two different design philosophies in the industry. Airbus uses a hard-limiting approach in which envelope limits cannot be exceeded, even with deliberate pilot input. The second approach, common in Boeing aircraft, is soft-limiting, which allows the pilot to override and exceed envelope limits. A great example of this difference is seen in bank angle protection. Typically, in Airbus aircraft, the bank angle is hard-limited to $\pm 66^\circ$ [26]. On the other hand, in Boeing aircraft, the bank angle is soft-limited to $\pm 35^\circ$. It is possible to steer the aircraft beyond this limit only by overcoming the additional control wheel force opposing the pilot. FEP systems on modern airliners generally include protections for angle of attack, bank angle, load factor, and pitch. In Airbus aircraft, the load factor and pitch are limited to -1g and -15°, nose down and 2.5g and 30°, nose up [27].

This study adopts a hybrid FEP approach that combines elements of both Airbus and Boeing methodologies. For example, bank protection enforces both soft and hard limits. On the other hand, the input device is a passive sidestick, similar to an Airbus aircraft in normal law. That is, unlike in Boeing aircraft, the input device does not create additional forces that the pilot must overcome after reaching the soft limit. The FEP system is particularly important for the Flying V to limit the angle of attack and avoid flight conditions that can cause longitudinal instability.

C. Incremental Nonlinear Dynamic Inversion

Control theory offers a wide array of tools to analyze and control linear systems. However, almost all real-life systems, including the Flying V, are nonlinear. A common aerospace approach to this problem is using nonlinear dynamic inversion (NDI), also known as feedback linearization [28]. NDI relies on model information to design a linearizing control law that cancels out nonlinearities. As a result, the performance of NDI strongly depends on model accuracy. An alternative formulation called incremental nonlinear dynamic inversion (INDI) reduces the reliance on model information. By replacing a part of the model with sensor feedback, INDI only requires a control effectiveness model to perform model inversion, canceling nonlinearities.

In recent years, INDI and its variants have been applied to the control of a variety of aerospace topics and systems, including helicopters, quadrotors, fighter jets, light business jets, flexible airplanes and other flying-wing aircraft [29–34]. In addition, many other studies have focused on fault-tolerant flight control [35–38].

Currently, INDI has been employed as the inner-loop controller for the Flying V in combination with FBW outer guidance loops [7, 9, 15]. This combination has shown promising results in improving handling qualities, tracking responses, and dealing with model uncertainties. However, as mentioned in Section I.A, there are a few issues that require further action.

D. Contributions and Paper Outline

The contributions of this paper are as follows. On a higher level, the paper addresses important issues in the existing Flying V control architecture [7], including pitch dropout, lack of pitch compensation during turns, overshoots in flight envelope protection response, and model fidelity limitations. This is accomplished by employing a cascaded control structure that consists of outer guidance loops based on relevant industry approaches and an inner inversion loop based on incremental nonlinear dynamic inversion. The outer loop includes a Boeing-inspired C*U for pitch control with speed stability, a rate command attitude hold (RCAH) controller along the roll channel that compensates for pitch during turns, and a sideslip controller that uses a feedback loop similar to nonlinear dynamic inversion. Furthermore, the study employs a recently developed aerodynamic model [4] synthesized using Vortex Lattice Method (VLM) and Reynolds-averaged Navier Stokes (RANS) simulations.

As part of the outer loop, this study designs a flight envelope protection system using command limiting exponential potential functions, which addresses the problem of overshoot in the FEP response and restricts the aircraft from reaching flight conditions that might cause longitudinal instability. The study extends the existing approach of command limiting with exponential potential functions in rate-controlled systems [39–41] to develop a comprehensive FEP architecture including angle of attack, bank angle, load factor, and pitch constraints.

Lastly, this study involves conducting piloted flight simulations with technical pilots from industry. Simulations focus on assessing handling qualities, certification compliance, and testing the effectiveness of the FEP system. These simulations are carried out in the SIMONA Research Simulator of Delft University of Technology [42].

The rest of the paper is structured as follows. Section II describes the Flying V simulation model including the control layout, aerodynamics, actuators, sensors, and engines. Section III presents the design and theory of normal law flight controls that cover the inner inversion loop, outer guidance loop, and flight envelope protection. Section IV explains the tuning process for the outer loop. Section V outlines the maneuver design, flight conditions, the SIMONA Research Simulator, and the participating pilots. Section VI presents the results and provides a detailed discussion. Lastly, Section VII reiterates contributions, summarizes key findings, and suggests directions for future research.

II. Description of the Flying V Model

In recent years, substantial efforts have been made to advance the technology readiness level (TRL) of the Flying V model. These efforts include developing new aerodynamic models based on subscale flight tests [10] and wind tunnel investigations [5, 11], designing flight control systems [7], and evaluating the handling qualities under both direct and normal flight laws [9, 12]. The current study focuses on flight control design and testing, as well as handling quality assessment under normal law. This section outlines the version of the Flying V simulation model used in this research. Figure 1 shows an illustration of the Flying V, together with its control surfaces. The elevons and rudders are used to control all three axes with a deflection proportional to their effectiveness, whereas the HLDs are manually deployed at low speeds.

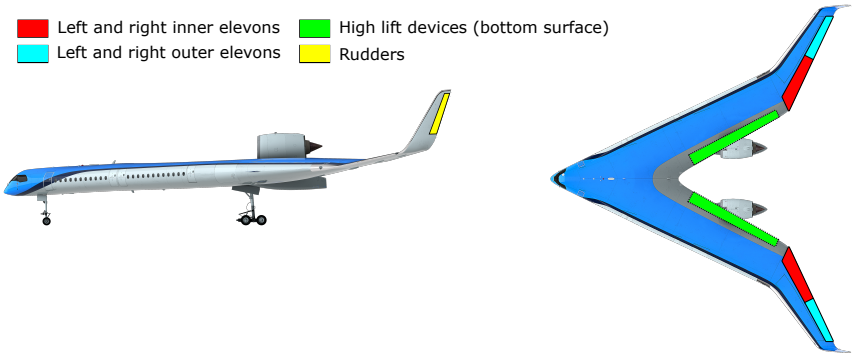

Fig. 1 Flying V with control surfaces

A. Aerodynamic Model

The full-scale aerodynamic model is derived from a combination of VLM and RANS simulations [4]. Static coefficients are obtained through RANS, dynamic coefficients are determined by calibrating VLM with subscale flight and wind tunnel test results, while control coefficients are calculated using VLM simulations calibrated with RANS. The reason for combining these methods stems from a trade-off between fidelity and computational cost. VLM assumes that the flow is inviscid, irrotational, and incompressible, making it a low-cost, low-fidelity method that is typically used to quickly obtain an aerodynamic model. However, these assumptions prevent VLM from predicting nonlinearities such as pitch break, transonic and crossflow effects, and nonlinear variations in control effectiveness with respect to angles of attack and sideslip [43]. In contrast, RANS is a higher fidelity method, capable of capturing various nonlinearities. The performance of RANS relative to other high-fidelity approaches like Direct Numerical or Large-Eddy Simulations depends largely on the mesh quality, with a finer mesh resulting in a high-fidelity, high-cost solution. Therefore, combining VLM with RANS allows for the development of nonlinear aerodynamic models at a lower cost. The control surfaces are sized and placed to meet specific certification requirements outlined in EASA's CS-25 initial airworthiness specifications [44] under direct flight law. This procedure and the rationale behind it are extensively explained in [4, 6].

The resulting aerodynamic model has a polynomial structure and captures nonlinearities such as pitch break and cross-dependencies between some of the terms. Table 1 outlines the dependency of each coefficient and the method used to generate them. In this table, R stands for RANS, V for VLM, V-R for VLM calibrated with RANS, α and β

Table 1 Coefficient dependencies, adopted from [6]

	Static		Dynamic			Control Surfaces		
Coefficients	α	$\beta(\alpha)$	$\hat{p}$	$\hat{q}$	$\hat{r}$	$\delta_e(\alpha)$	$\delta_r(\alpha)$	$\delta_{HLD}(\alpha)$
C_X	R					V-R	V-R	V-R
C_Y		R			V	V-R	V-R	
C_Z	R			V		V-R		V-R
C_L		R	V		V	V-R	V-R	
C_M	R			V		V-R		V-R
C_N		R	V		V	V-R	V-R	

are angles of attack and sideslip, $\hat{p}, \hat{q}, \hat{r}$ are dimensionless angular rates, δ_e represents elevon deflections, δ_r rudder deflections, and δ_{HLD} high-lift device deflections. The terms with (α) next to them means that their impact on the coefficients is influenced by the angle of attack. Lastly, C_X, C_Y, C_Z are the force coefficients along X, Y, and Z, while C_L, C_M, C_N are the roll, pitch and yaw moment coefficients, respectively. The aerodynamic model development for the Flying V is an ongoing research activity. Therefore, the model presented in Table 1 represents the current state and is open to future changes.

B. Actuators and Engines

The Flying V model in this study features four elevons and two coupled rudders as primary control surfaces, in addition to two high-lift flaps, as shown in Figure 1. The Flying V uses fewer but larger control surfaces compared to existing commercial aircraft with similar wingspan. For example, the Airbus A350-1000 has 22 primary surfaces, (4 ailerons, 14 spoilers, 2 elevators, 1 rudder, 1 horizontal stabilizer) [45]. This deviation from traditional designs is primarily due to the evolving control layout of the Flying V and the unconventional control requirements of flying wings. The possibility of adding split flaps, drag rudders, and flaperons is an active research topic for the Flying V.

In this paper, the elevon and rudder actuators are modeled as second-order systems. High-lift flaps are assumed to automatically deflect at low speeds, so when they are needed, the trim is calculated with them already deployed. Therefore, these surfaces do not have transient dynamics. The engines are modeled as first-order systems and are based on the Rolls-Royce Trent XWB-84 with thrust specifications available in [46]. The actuator and engine dynamics are selected as follows:

$$H_{\text{act}}(s) = \frac{\omega_n^2}{s^2 + 2\zeta\omega_n s + \omega_n^2} \quad \text{and} \quad H_{\text{eng}}(s) = \frac{1}{\tau s + 1} \tag{1}$$

where ω_n is the natural frequency, ζ damping ratio, and τ time constant. The actuator sensors that measure actuator deflections, H_{as}, are modeled as second-order systems similar to H_{act}. The previous actuator models used in Flying V

control design and handling quality studies are based on military aircraft. As a result, they have fast dynamics with high rate limits. However, this is not accurate for a commercial aircraft with relatively large surfaces. The selection of natural frequency and damping terms must take this into account. Based on [47], the Boeing 747 simulation model uses a natural frequency of 35 rad/s and a damping ratio of 0.8 for the aileron actuators. Furthermore, according to [48], choosing a natural frequency of 20 rad/s and a damping ratio of 1, leads to a bandwidth that closely approximates electromechanical actuator servos. Based on this, to choose a conservative bandwidth, the natural frequency and damping ratio are set as $\omega_n = 10$ rad/s and $\zeta = 1$, respectively, together with a engine time constant of $\tau = 0.2$ s.

Furthermore, actuator rate limits should also be adjusted to better reflect commercial aircraft. Another Boeing 747 simulation model from NASA [49] considers a rate limit of 55 deg/s for ailerons and 37 deg/s for elevators. Since the Flying V uses elevons instead of dedicated elevators and ailerons, they must perform both roles. Hence, the elevons should match the faster dynamics and larger deflection limits of the ailerons. Based on this, the deflection and rate limits are given in Table 2.

Table 2 Control surface operating ranges

Control Surface	δ_{cs}, deg	$\dot{\delta}_{cs}$, deg/s
Elevons	$[-25, 25]$	$[-55, 55]$
Rudders	$[-30, 30]$	$[-40, 40]$
High Lift Device	$[0, 40]$	–

C. Sensors

The sensors of the Flying V model are chosen from a set of commercially available alternatives. This includes a navigation-grade IMU that is certified to operate without GPS/GNSS assistance with three state-of-the-art gyroscopes and accelerometers [¶]. The system also features a combined GNSS/INS package that provides airspeed and attitude angles [‖], and a separate GNSS receiver that measures groundspeed [**]. In addition, an air data system is included based on Cessna Citation II PH-LAB [50], a research aircraft jointly operated by NLR and Delft University of Technology. Table 3 provides an overview of the sensor characteristics.

Table 3 Sensor characteristics, adopted from [15]

Measurements	Update Rate, Hz	Standard Deviation, σ	Unit
$u_{GS_m}, v_{GS_m}, w_{GS_m}$	10	0.030	m/s
V_{t_m}	100	0.005	m/s
α_m, β_m	100	$2.7 \cdot 10^{-4}$	rad
ϕ_m, θ_m	100	$8.7 \cdot 10^{-5}$	rad
ψ_m	100	$1.7 \cdot 10^{-4}$	rad
A_{xm}, A_{ym}, A_{zm}	100	$6.9 \cdot 10^{-4}$	m/s^2
p_m, q_m, r_m	100	$4.1 \cdot 10^{-6}$	rad/s

III. Flight Control Laws

The common industry approach to flight control design is developing redundant control laws of varying augmentation levels. A certified commercial aircraft generally includes three types of control laws: normal, alternate (secondary), and direct. The normal law is a highly augmented fly-by-wire control law that utilizes a wide range of sensors and

[¶] https://aerospace.honeywell.com/us/en/products-and-services/products/navigation-and-sensors/inertial-measurement-units/hg9900-inertial-measurement-unit [Accessed: May 19, 2025]

[‖] https://www.advancednavigation.com/inertial-navigation-systems/fog-gnss-ins/boreas/d90-datasheet/ [Accessed: May 19, 2025]

[**] https://www.unmannedsystemstechnology.com/company/honeywell/hguide-g080-gnss-receiver/ [Accessed: May 19, 2025]

model information. It is typically used as the default flight control law. This control mode uses flight computers to interpret pilot inputs and calculate the necessary control surface deflections, acting as a bridge between the pilot and the control actuators. The alternate or secondary law is similar to the normal law; however, with reduced capabilities. For example, the secondary law of the Boeing 777 does not include flight envelope protection [17]. Lastly, the direct law refers to minimal control and stability augmentation. This control mode uses either very limited or no sensor and model information. Unlike normal and alternate laws, in direct law, the pilot inputs are simply distributed over the control actuators, without relying on any additional sensor inputs.

The rationale behind designing a spectrum of flight controllers is for safety. Although the normal law is quite capable of stabilizing and improving handling of aircraft, it is dependent on sensors. Consequently, if some sensors malfunction during flight, continuing flight with normal law can compromise flight safety. For this reason, it is mandatory for all aircraft to have an operational direct law as a contingency to meet certification requirements. Moreover, to further the commercialization efforts of the Flying V, this study sets handling quality targets for direct and normal flight laws. The established targets are Level 1 for the normal law and Level 2 for the direct law. This section focuses on the theory and design of normal flight control laws.

A. Overview of Normal Flight Law

Normal flight law consists of a comprehensive stability and control augmentation system, entailing a cascaded inner and outer loop structure. Cascaded design enables the separation of the flight control problem into an outer loop that is handling quality dependent, and an inner loop contingent on airframe stability. The inner loop employs incremental nonlinear dynamic inversion in conjunction with a control allocation algorithm based on generalized pseudoinverse, while the outer loop utilizes industry-inspired fly-by-wire control laws. The inner loop uses an onboard model (OBM) containing the control effectiveness matrix of the aircraft at different flight conditions for dynamic inversion. The outer loop is gain-scheduled at different flight conditions to maintain consistent performance across the flight envelope. Figure 2 shows the complete cascaded control architecture. This section dives into the details of this architecture, starting with the inner loop.

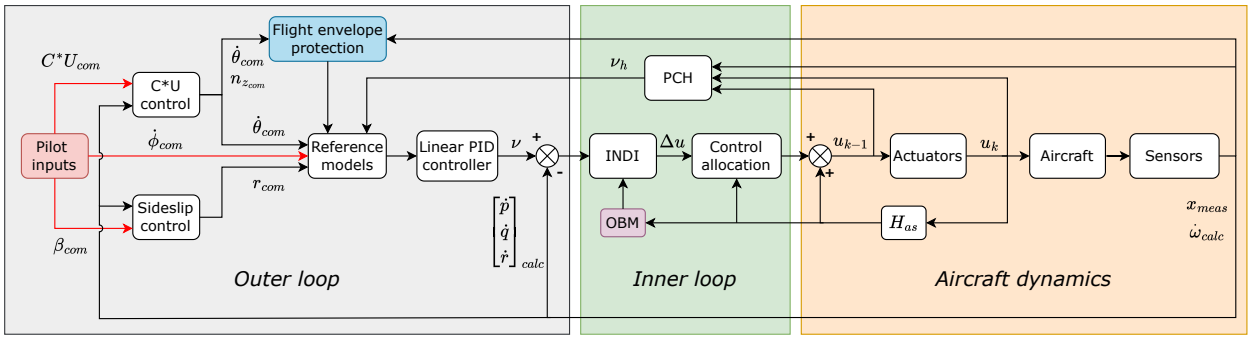

Fig. 2 Normal flight law control architecture

B. Incremental Nonlinear Dynamic Inversion

Incremental nonlinear dynamic inversion is a form of feedback linearization. Using both sensors and partial model information, INDI effectively linearizes nonlinear systems. This allows for the application of linear control techniques to nonlinear systems like the Flying V. In the context of flight control, a model generally refers to the aerodynamic data related to the actual aircraft, such as force and moment coefficients, while the sensors are part of the system dynamics and specific to the airframe. This section provides some theoretical background on (I)NDI and formulates it as a technique for angular rate control.

Assume the nonlinear system is given in Eqs. (2) and (3) is control affine.

$$\dot{\boldsymbol{x}} = \mathbf{f}(\boldsymbol{x}) + \mathbf{G}(\boldsymbol{x})\boldsymbol{u} \tag{2}$$

$$\boldsymbol{y} = \mathbf{h}(\boldsymbol{x}) \tag{3}$$

where $\boldsymbol{x}$ is the $l \times 1$ state vector, $\boldsymbol{u}$ is the $m \times 1$ input vector, and $\boldsymbol{y}$ is the $n \times 1$ output vector, with l, m, n number of states, inputs, and outputs, respectively [28]. Fundamentally, the goal of nonlinear dynamic inversion is finding a relationship between the input and the desired output such that it can be inverted, enabling the computation of the input required to achieve the desired system behavior. The relationship is obtained by differentiating the output equation until the input appears. This results in the following:

$$\dot{\boldsymbol{y}} = \frac{\partial \mathbf{h}(\boldsymbol{x})}{\partial \boldsymbol{x}} \frac{\mathrm{d}\boldsymbol{x}}{\mathrm{d}t} = \nabla \mathbf{h}(\boldsymbol{x}) \dot{\boldsymbol{x}} = \nabla \mathbf{h}(\boldsymbol{x}) [\mathbf{f}(\boldsymbol{x}) + \mathbf{G}(\boldsymbol{x}) \boldsymbol{u}] \tag{4}$$

where ∇ is the gradient operator. In this expression, the input $\boldsymbol{u}$ appears as a function of $\dot{\boldsymbol{y}}$, indicating that the relationship is found. In cases where a single differentiation does not reveal the input, determining the relationship requires higher-order differentiation. It is possible to reformulate and simplify Eq. (4) using Lie derivatives. The first-order Lie derivative along $\mathbf{f}(\boldsymbol{x})$ is defined as $L_f \mathbf{h}(\boldsymbol{x}) = \nabla \mathbf{h}(\boldsymbol{x}) \mathbf{f}(\boldsymbol{x})$. Similarly, the first-order Lie derivative along $\mathbf{G}(\boldsymbol{x})$ is $L_g \mathbf{h}(\boldsymbol{x}) = \nabla \mathbf{h}(\boldsymbol{x}) \mathbf{G}(\boldsymbol{x})$. Rewriting Eq. (4) leads to

$$\dot{\boldsymbol{y}} = L_f \mathbf{h}(\boldsymbol{x}) + L_g \mathbf{h}(\boldsymbol{x}) \boldsymbol{u} \tag{5}$$

Now, by inverting the equation, it is possible to obtain the linearizing input.

$$\boldsymbol{u} = L_g \mathbf{h}^{-1}(\boldsymbol{x}) (\boldsymbol{\nu} - L_f \mathbf{h}(\boldsymbol{x})) \tag{6}$$

It may be observed that the derivative of the system output $\dot{\boldsymbol{y}}$ is substituted by a pseudocontrol input, $\boldsymbol{\nu}$ that represents the desired system behavior. Consequently, Eq. (6) effectively computes the input necessary to obtain the desired behavior. For the purposes of our application, $\boldsymbol{\nu}$ comes from a linear PID controller, as shown in Figure 2.

So far, the section has introduced the theory of nonlinear dynamic inversion in a general sense. The next step is to apply this to aircraft angular rate control. Based on [28], choosing angular rates as controlled variables $\mathbf{h}(\boldsymbol{x}) = \boldsymbol{\omega}$ and differentiating the output equation results in

$$\dot{\boldsymbol{\omega}} = \mathbf{I}^{-1} (\mathbf{M}_s + \mathbf{M}_{\boldsymbol{\delta}} \boldsymbol{\delta} - \boldsymbol{\omega} \times \mathbf{I} \boldsymbol{\omega}) \tag{7}$$

where $\mathbf{I}$ is the moment of inertia matrix, $\mathbf{M}_s$ the part of the aerodynamic model that depends on stability derivatives, $\mathbf{M}_{\boldsymbol{\delta}}$ contains the control coefficients, and $\boldsymbol{\delta}$ represents control deflections, i.e., system input, $\boldsymbol{u}$. Formulating the equation in this way allows for splitting the aerodynamic model into two as stability- and control-dependent components. Rewriting Eq. (7) in the form of Eq. (6) leads to

$$\boldsymbol{\delta} = (\mathbf{M}_{\boldsymbol{\delta}})^{-1} (\mathbf{I} \boldsymbol{\nu} + \boldsymbol{\omega} \times \mathbf{I} \boldsymbol{\omega} - \mathbf{M}_s) \tag{8}$$

This NDI law depends on the entire aerodynamic model. As a result, the control law is affected by model mismatches in all elements of the aerodynamic data.

A possible method to reduce this dependency is to reformulate NDI in an incremental form, leading to incremental NDI. The first step toward this is rewriting the rotational accelerations, $\dot{\boldsymbol{\omega}}$, in an incremental form. Following [28, 51], this can be done by taking a first-order Taylor series expansion of Eq. (7) as

$$\begin{aligned} \dot{\boldsymbol{\omega}} \approx \dot{\boldsymbol{\omega}}_0 &+ \frac{\partial}{\partial \boldsymbol{\omega}} \left[\mathbf{I}^{-1} (\mathbf{M}_s + \mathbf{M}_{\boldsymbol{\delta}} \boldsymbol{\delta} - \boldsymbol{\omega} \times \mathbf{I} \boldsymbol{\omega}) \right]_{\boldsymbol{\omega} = \boldsymbol{\omega}_0, \boldsymbol{\delta} = \boldsymbol{\delta}_0} (\boldsymbol{\omega} - \boldsymbol{\omega}_0) \\ &+ \frac{\partial}{\partial \boldsymbol{\delta}} \left[\mathbf{I}^{-1} (\mathbf{M}_s + \mathbf{M}_{\boldsymbol{\delta}} \boldsymbol{\delta} - \boldsymbol{\omega} \times \mathbf{I} \boldsymbol{\omega}) \right]_{\boldsymbol{\omega} = \boldsymbol{\omega}_0, \boldsymbol{\delta} = \boldsymbol{\delta}_0} (\boldsymbol{\delta} - \boldsymbol{\delta}_0) \end{aligned} \tag{9}$$

At this stage, it is possible to simplify this expression by employing the time scale separation principle. Given that this Taylor series expansion approximates angular accelerations, the influence of the third term on the right-hand side is considerably greater than that of the second term. This follows from the fact that a change in control deflections, $\boldsymbol{\delta} - \boldsymbol{\delta}_0$, immediately impacts moments and, by extension, angular accelerations. A change in angular rates $\boldsymbol{\omega} - \boldsymbol{\omega}_0$, on the other hand, takes time to develop as a response to changes in accelerations. As a result, at each time step, from the perspective of control deflections, angular rates can be seen as constant. This assumption holds as long as control actuators are sufficiently fast. Based on this, defining $\mathrm{d}\boldsymbol{\delta} = \boldsymbol{\delta} - \boldsymbol{\delta}_0$, the rotational acceleration is written in Eq. (10).

$$\dot{\boldsymbol{\omega}} = \dot{\boldsymbol{\omega}}_0 + \mathbf{I}^{-1} \mathbf{M}_{\boldsymbol{\delta}} \mathrm{d}\boldsymbol{\delta} \tag{10}$$

Lastly, applying $\boldsymbol{\nu}$ and inverting the equation, the final linearizing law is obtained as

$$\mathrm{d}\boldsymbol{\delta} = (\mathbf{M}_{\boldsymbol{\delta}})^{-1}\mathbf{I}(\boldsymbol{\nu} - \dot{\boldsymbol{\omega}}_0) \tag{11}$$

In practice, the current total deflection is obtained by adding this increment to the previous total deflection, $\boldsymbol{\delta}(t_k) = \boldsymbol{\delta}(t_{k-1}) + \mathrm{d}\boldsymbol{\delta}$.

Looking at Eq. 11, the advantage of INDI over NDI becomes clear, as this equation does not depend on the complete aerodynamic model but only on control coefficients. This makes INDI more robust against model uncertainties. However, the INDI formulation assumes that $\dot{\boldsymbol{\omega}}_0$ is available either directly through sensor measurements or can be calculated from them.

Applying this linearizing law to the Flying V introduces a challenge when inverting the control effectiveness matrix, $\mathbf{M}_{\boldsymbol{\delta}}$. The Flying V, as illustrated in Figure 1, features six primary control surfaces: four elevons and two rudders. The rudders are coupled and counted as a single actuator, leading to a total of five independent actuators. Implementing the INDI law to control all three angular rates around roll, pitch, and yaw axes, leads to a 3×5 control effectiveness matrix, creating an under-determined system with infinitely many solutions. Solving for this under-determined system by inverting the control effectiveness matrix requires employing control allocation techniques, as discussed in the following subsection.

C. Control Allocation

Aircraft are typically rotationally over-actuated, meaning they possess more control effectors than required to manipulate the roll, pitch, and yaw axes. Consequently, when allocating control moments over available surfaces, the resulting problem becomes inherently under-determined, offering multiple valid solutions to achieve the same desired rotational effect. In flight control, this creates both a challenge and an opportunity. It is a challenge in the sense that when dealing with highly over-actuated systems like the Airbus A350 with 22 primary control effectors, the control allocation problem becomes increasingly complex. However, it is also an opportunity because redundant surfaces can be utilized to meet secondary objectives using optimization algorithms [52].

A promising algorithm that minimizes the sum of squares of control deflections is called Cascaded Generalized Inverses [53]. It has been applied on the previous Flying V models with success [7, 15] and on Lockheed Martin's X-35B [54]. This algorithm relies on a minimum-norm pseudoinverse to minimize $\boldsymbol{\delta}^T\boldsymbol{\delta}$ under the constraint $\mathbf{M}_{\boldsymbol{\delta}}\boldsymbol{\delta} = \boldsymbol{m}$. Using Lagrange multipliers allows defining the function given in Eq. (12).

$$\boldsymbol{L}(\boldsymbol{\delta}, \boldsymbol{\lambda}) = \frac{1}{2}\boldsymbol{\delta}^T\boldsymbol{\delta} + \boldsymbol{\lambda}^T(\boldsymbol{m} - \mathbf{M}_{\boldsymbol{\delta}}\boldsymbol{\delta}) \tag{12}$$

where $\boldsymbol{\lambda}$ is a vector of Lagrange multipliers. For $\boldsymbol{L}(\boldsymbol{\delta}, \boldsymbol{\lambda})$ to be minimized, the following equalities must be satisfied.

$$\frac{\partial \boldsymbol{L}}{\partial \boldsymbol{\delta}} = \mathbf{0} = \boldsymbol{\delta}^T - \boldsymbol{\lambda}^T\mathbf{M}_{\boldsymbol{\delta}}, \quad \frac{\partial \boldsymbol{L}}{\partial \boldsymbol{\lambda}} = \mathbf{0} = \boldsymbol{m} - \mathbf{M}_{\boldsymbol{\delta}}\boldsymbol{\delta} \tag{13}$$

which leads to $\boldsymbol{\delta} = \mathbf{M}_{\boldsymbol{\delta}}^T\boldsymbol{\lambda}$ and $\boldsymbol{m} = \mathbf{M}_{\boldsymbol{\delta}}\boldsymbol{\delta}$. Combining these and solving for $\boldsymbol{\lambda}$ yields

$$\boldsymbol{\lambda} = \left(\mathbf{M}_{\boldsymbol{\delta}}\mathbf{M}_{\boldsymbol{\delta}}^T\right)^{-1}\boldsymbol{m} \tag{14}$$

Lastly, inserting Eq. (14) back into $\boldsymbol{\delta} = \mathbf{M}_{\boldsymbol{\delta}}^T\boldsymbol{\lambda}$ gives the final expression as:

$$\boldsymbol{\delta} = \mathbf{M}_{\boldsymbol{\delta}}^T\left(\mathbf{M}_{\boldsymbol{\delta}}\mathbf{M}_{\boldsymbol{\delta}}^T\right)^{-1}\boldsymbol{m} \tag{15}$$

where pseudoinverse is $\mathbf{M}_{\boldsymbol{\delta}}^p = \mathbf{M}_{\boldsymbol{\delta}}^T(\mathbf{M}_{\boldsymbol{\delta}}\mathbf{M}_{\boldsymbol{\delta}}^T)^{-1}$. Hence, applying this pseudoinverse simultaneously solves the control allocation problem while minimizing $\boldsymbol{\delta}^T\boldsymbol{\delta}$, which is a measure of control effort [53]. Consequently, the INDI law defined in Eq. 11, now becomes

$$\mathrm{d}\boldsymbol{\delta} = (\mathbf{M}_{\boldsymbol{\delta}}^p)\mathbf{I}(\boldsymbol{\nu} - \dot{\boldsymbol{\omega}}_0) \tag{16}$$

For in-depth details about the cascaded structure and the logic for dealing with saturation, the reader is referred to [7, 53].

D. Pseudo Control Hedging

Pseudo Control Hedging (PCH) is a technique that was originally developed in [55] as a method to deal with actuator saturation in adaptive control. Saturation causes the system to be non-affine in the input, which invites controllability and invertibility issues. The latter is highly relevant for dynamic inversion-based controllers. Although INDI inverts aircraft dynamics, it does not account for control actuators. In simulation models, actuators are often represented as first- or second-order systems, which introduce time delays and transient dynamics to the input signal. These dynamics can create performance degradation in INDI control laws [29].

This section introduces PCH for actuator compensation by correcting the reference model. Recall the pseudocontrol expression derived for the INDI law:

$$\boldsymbol{\nu} = \dot{\boldsymbol{\omega}}_0 + \mathbf{I}^{-1}\mathbf{M}_{\boldsymbol{\delta}}(\boldsymbol{\delta} - \boldsymbol{\delta}_0) \tag{17}$$

$\boldsymbol{\delta}$ corresponds to the commanded control deflections that act as input to the actuators, shown as $\boldsymbol{u}_{k-1}$ in Figure 2. By taking measurements of the actual control deflections, $\boldsymbol{\delta}_{act}$, shown as $\boldsymbol{u}_k$, it is possible to estimate a virtual control as

$$\hat{\boldsymbol{\nu}} = \dot{\boldsymbol{\omega}}_0 + \mathbf{I}^{-1}\mathbf{M}_{\boldsymbol{\delta}}(\boldsymbol{\delta}_{act} - \boldsymbol{\delta}_0) \tag{18}$$

The virtual hedge $\boldsymbol{\nu}_h$, then can be calculated by taking the difference of these two virtual controls.

$$\boldsymbol{\nu}_h = \boldsymbol{\nu} - \hat{\boldsymbol{\nu}} = \left(\dot{\boldsymbol{\omega}}_0 + \mathbf{I}^{-1}\mathbf{M}_{\boldsymbol{\delta}}(\boldsymbol{\delta} - \boldsymbol{\delta}_0)\right) - \left(\dot{\boldsymbol{\omega}}_0 + \mathbf{I}^{-1}\mathbf{M}_{\boldsymbol{\delta}}(\boldsymbol{\delta}_{act} - \boldsymbol{\delta}_0)\right) \tag{19}$$

This leads to the final expression given in Eq. (20).

$$\boldsymbol{\nu}_h = \mathbf{I}^{-1}\mathbf{M}_{\boldsymbol{\delta}}(\boldsymbol{\delta} - \boldsymbol{\delta}_{act}) \tag{20}$$

Assuming a first-order reference model, and feeding the virtual hedge back leads to

$$\boldsymbol{\omega}_{rm} = \frac{1}{s}(\dot{\boldsymbol{\omega}}_{rm} - \boldsymbol{\nu}_h) \tag{21}$$

where the subscript rm stands for the reference model. Hence, in case of control saturation, by essentially hedging $\dot{\boldsymbol{\omega}}_{rm}$, reference commands are brought down to a level achievable by the actuators. If there is no saturation, $\boldsymbol{\delta} \approx \boldsymbol{\delta}_{act}$, then $\boldsymbol{\nu}_h \approx \mathbf{0}$, leaving the reference model nearly untouched. However, it is still affected by the differences in commanded and actual deflections due to the time lag caused by actuator dynamics.

E. Longitudinal Control and C*U Parameter

C* parameter was designed as handling quality criterion in the 1960s. In its pure form, it is expressed as a linear combination of pitch rate and load factor at the pilot station. The concept is based on the assumption that pilots perceive and respond to cues related to both load factor and pitch rate [20]. Furthermore, it is presumed that pitch rate cues are dominant at lower speeds and load factor cues at higher speeds. This is a logical argument as an identical pitch rate results in a larger change in load factor at higher speeds. The pure C* is given is Eq. (22).

$$\mathrm{C}^* = n_{z,pilot} + \frac{V_{CO}}{g}q \tag{22}$$

where $n_{z,pilot}$ is the load factor at the pilot station and V_{CO} is the crossover velocity, representing a unique velocity at which pitch rate and load factor contribute equally to the C* parameter. V_{CO} is chosen as 130 m/s [18, 20] for the Flying V simulation model used in this study.

Since its conception, C* has evolved into an umbrella term for fly-by-wire longitudinal control methods that employ a combination of pitch rate and load factor. Currently, different forms of C* are deployed in many active commercial aircraft. For instance, Airbus uses the parameter closer to its pure form, while Boeing favors a modified C*U parameter with speed stability [19]. An approach similar to Airbus has been previously used in longitudinal flight laws of the Flying V, and tested in the simulator [7, 15]. However, this study employs a C*U method closer to Boeing aircraft, given in Eq. (23).

$$(\mathrm{C}^*\mathrm{U})_{ss}\frac{\cos(\theta_{trim} - \theta)}{\cos\phi} = n_{z_{pilot}} + \frac{V_{CO}}{g}q + (V - V_{com})K_V \tag{23}$$

$(\mathrm{C}^*\mathrm{U})_{ss}$ on the left side of Eq. 23 is the quantity commanded by the pilot using sidestick inputs, while $\cos(\theta_{trim}-\theta)/\cos\phi$ scales this input for turn compensation and accounts for the pitch required for trimming. On the other hand, the right

side represents a target quantity to be achieved in response to the pilot's stick inputs. V and V_{com} are the actual and commanded speeds of the aircraft, respectively. The advantage of this structure is the additional speed stability. When the aircraft speed V is below the commanded speed V_{com}, the C*U parameter decreases, causing a pitch down until speed is regained. Conversely, the aircraft pitches up when V exceeds V_{com}. It is important to note that this automatic pitching action does not move the sidestick control inceptor employed in this study, which is different from the active/backdriven inceptors used in Boeing aircraft.

Now, by defining the compensated C*U as

$$(\mathrm{C^*U})_{comp} = (\mathrm{C^*U})_{ss} \frac{\cos(\theta_{trim} - \theta)}{\cos\phi} \tag{24}$$

the load factor can be isolated to incorporate flight envelope protection and compute a pitch rate for the reference model.

$$n_{z,com} = (\mathrm{C^*U})_{comp} - \frac{V_{CO}}{g} q_m - (V - V_{com}) K_V \tag{25}$$

where $n_{z,com}$ is the commanded load factor and q_m is the measured pitch rate. As explained in a later subsection, the FEP on angle of attack and load factor is applied on $n_{z,com}$. Subsequently, the error dynamics of the load factor are obtained as

$$e_{n,z} = n_{z,com} - n_{z,m} \tag{26}$$

where $n_{z,m}$ is the measured load factor. At this stage, a discrete PI controller is utilized to compute the pitch rate using the expression given in Eq. (27).

$$\dot{\theta}_{com} = \left[K_p e_{n,z} + \frac{K_i T_s}{z-1} e_{n,z} + K_f (n_{z,com} - 1) \right] + \dot{\theta}_{comp} \tag{27}$$

T_s is the controller sampling time and it is set to 100 Hz for this study. The final component of the longitudinal controller is the term $\dot{\theta}_{comp}$, given in Eq. (28).

$$\dot{\theta}_{comp} = (\theta_{target} - \theta) \left(K_p + K_i \frac{T_s}{z-1} \right) \tag{28}$$

This term assists the rate command attitude hold controller by maintaining pitch attitude during turns. When the pilot initiates a pure roll maneuver, this component preserves the aircraft's most recent pitch attitude. Commanding a new pitch angle during a roll disables this element, giving the pilot full manual control over pitch.

F. Reference Model and RCAH Control

The roll control channel consists of two components. First is a command filter with bank protection that enforces envelope protection limits and integrates the pilot roll rate input, $\dot{\phi}_{com}$. This is followed by a second-order reference model that takes the limited roll rate $\dot{\phi}_{prot}$ and the commanded roll ϕ_{com} as inputs. Figure 3 depicts the reference model structure in discrete form. The subscript m refers to the measured angles, and $\nu_{h,\dot{p}}$ is the virtual hedge for the roll

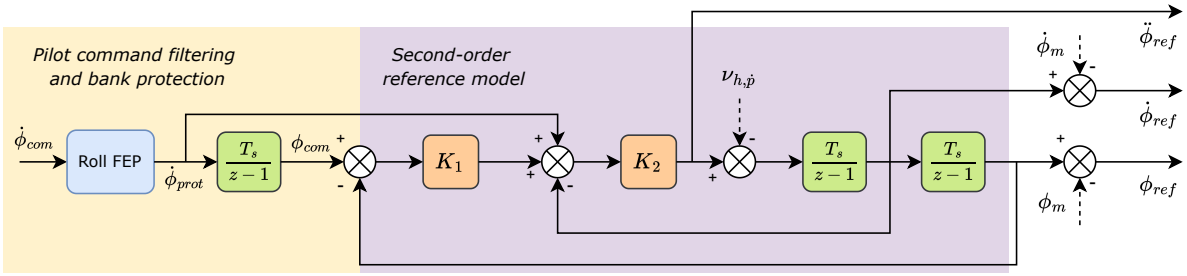

Fig. 3 Roll reference model with command filtering

acceleration as defined in Eq. (21). The final references ϕ_{ref}, $\dot{\phi}_{ref}$, and $\ddot{\phi}_{ref}$ are used in a PID based linear controller to calculate the virtual control used in Eq. (11). By using both roll and roll rate as inputs, the reference model functions

similarly to a rate command attitude hold controller, responding to roll rate but holding the roll position once the input stops. This characteristic in combination with the pitch hold element described in the previous subsection, forms the complete RCAH that maintains both pitch and roll angles.

The pitch reference model and command filter differ slightly from the one discussed here. First, the model accepts pitch rate commands $\dot{\theta}_{com}$, which are generated by the C*U controller. Second, instead of roll FEP, it contains load factor and angle of attack protections and generates pitch reference signals instead of roll. Therefore, this model is not presented in a separate figure for conciseness.

G. Sideslip Controller

As previously mentioned, the inner loop INDI controller is designed for rotational rate control. However, in line with industry applications, the directional channel is designed for sideslip control, allowing the pilot to command sideslip using pedal inputs. This creates an inconsistency between outer and inner loop interpretations of directional motion. Therefore, it is necessary to establish a relationship between sideslip angle and yaw rate. According to [56], this can be achieved by using a manual NDI-based feedback loop. The present study proposes a modified approach similar to the one described in [57], but in discrete form. Figure 4 shows the structure of the control channel. x_m are measured states

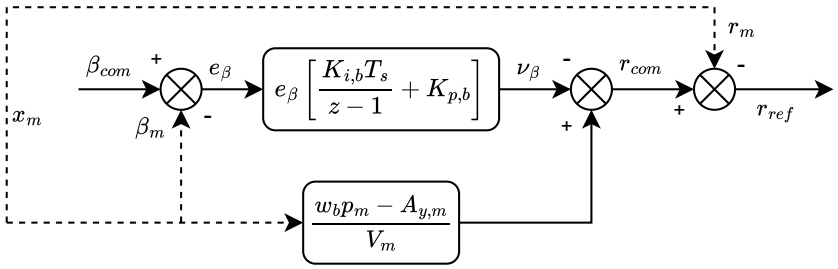

Fig. 4 Sideslip directional control

and β_{com} is the commanded sideslip through pedal inputs. This control design calculates a reference yaw rate using sensor data and a discrete PI structure. It is possible to express the controller in reduced form as in Eq. (29).

$$r_{ref} = \left[\frac{w_b p_m - A_{y,m}}{V_m} - (\beta_{com} - \beta_m)\left(\frac{K_{i,b}T_s}{z-1} + K_{p,b}\right)\right] - r_m \tag{29}$$

where w_b is the vertical true airspeed of the aircraft measured using air data sensors.

H. Linear Controller

Referring to Figure 2 and following the INDI derivation, the calculated rotational rate references are processed through a PID controller to determine the pseudo control input for model inversion. The linear controller consists of proportional-integral elements in discrete form, given as in Eqs. (30-32) for all rotational accelerations.

$$\nu_p = K_{p,\ddot{\phi}}\left(\ddot{\phi}_{ref}\right) + K_{p,\dot{\phi}}\left(\dot{\phi}_{ref}\right) + \left(\frac{K_{i,\phi}T_s}{z-1} + K_{p,\phi}\right)\left(\phi_{ref}\right) \tag{30}$$

$$\nu_q = K_{p,\ddot{\theta}}\left(\ddot{\theta}_{ref}\right) + K_{p,\dot{\theta}}\left(\dot{\theta}_{ref}\right) + K_{p,\theta}\left(\theta_{ref}\right) \tag{31}$$

$$\nu_r = K_{p,\beta}\left(r_{ref}\right) \tag{32}$$

Hence, in alignment with Eq. (11), $\boldsymbol{\nu} = \dot{\boldsymbol{\omega}} = \begin{bmatrix}\nu_p & \nu_q & \nu_r\end{bmatrix}^T$.

I. Flight Envelope Protection

It is known that flying wing aircraft, including the Flying V, have reduced longitudinal stability because they lack horizontal stabilizers. In fact, a few studies in the past concluded that the Flying V models synthesized with high-fidelity simulation methods exhibit pitch break behavior [4, 13]. This makes an effective flight envelope protection a vital component of the normal law for the Flying V. To this end, we present a command limiting FEP design using exponential

potential functions. Recently, a simpler version of this was implemented in an earlier Flying V model as described in [14]. The present study extends these concepts to an industry-relevant FEP architecture that includes angle of attack, bank angle, load factor, and pitch protections, validated through piloted real-time simulations. It is important to mention that the experiment design in Section V limits validation to angle of attack and bank angle protections, as the pitch and load factor limits are not expected to be reached before the angle of attack limit. This also ensures sufficient time for handling quality and certification maneuvers.

1. Theoretical Derivation

The stability proofs of this approach have been established in [40, 41] together with some preliminary applications to pitch and roll limiting. The formulation assumes that the aerial vehicle is equipped with rate control systems. This is especially attractive for the INDI-based inner loop angular rate controller implemented in this research. One key advantage of this method is that envelope prediction is not required. The core idea is to design a protection command that regulates the states of interest by limiting commanded references. Consider the following nonlinear system:

$$\dot{x}_1(t) = x_2(t) \tag{33}$$

$$\dot{x}_2(t) = f(x_2(t), r_u(t), t) \tag{34}$$

with $x_1(t)$ is the protected state, $x_2(t)$ is the rate of the protected state, and $r_u(t)$ is the limited pilot reference input. Defining $r_u(t)$ and $x_2(t)$ as

$$r_u(t) = r(t) + u_p(t) \tag{35}$$

$$x_2(t) = r_u(t) + e_r(t) \tag{36}$$

$r(t)$ is the reference input commanded by the pilot, u_p is the protection command limiting the reference input, and $e_r(t)$ is the controller tracking error for the reference input. Based on [40], two assumptions are necessary to ensure stability.

Assumption 1 *$r(t)$ is continuous and bounded with $r_n \leq r(t) \leq r_p$, $r_n < 0$ and $r_p > 0$.*

Assumption 2 *$x_2(t)$ is bounded-input bounded-output stable, meaning that rate commands have bounded error dynamics with satisfactory transient performance, i.e. $|e_r| < k$, $k > 0$.*

Fundamentally, these assumptions suggest that the pilot inputs should remain continuous and bounded, while the rate controller needs to guarantee adequate tracking.

Now that the system and assumptions are defined, the next step involves deriving the protection command. Consider an exponential potential function of the following form:

$$U_p^+(x_1(t), x_2(t)) = e^{\eta(x_1(t) - X_{lim} + \xi x_2(t))} \tag{37}$$

where X_{lim} is the protection limit of state $x_1(t)$ whereas η and ξ are design parameters that affect the smoothness of the limiting. Applying gradient descent yields

$$u_p^+(t) = \mathrm{a}(t)\frac{\partial U_p^+}{\partial x_1} = \mathrm{a}(t)\eta e^{\eta(x_1(t) - X_{lim} + \xi x_2(t))} \tag{38}$$

Choosing $\mathrm{a}(t) = -r(t)/\eta$ gives the protection command as in Eq. (39).

$$u_p^+(t) = -r(t)e^{\eta(x_1(t) - X_{lim} + \xi x_2(t))} \tag{39}$$

This consequently results in the final restricted command expressed as:

$$r_u(t) = r(t) + u_p^+(t) = r(t)\left(1 - e^{\eta(x_1(t) - X_{lim} + \xi x_2(t))}\right) \tag{40}$$

The severity of the correction depends significantly on the proximity of state $x_1(t)$ to its limit X_{lim}. When distant from the limit, the impact remains minimal; however, as the state approaches the limit, the correction becomes exponentially stronger. The protection command given in Eq. (39) represents a positive limiting. Following a similar logic, it is possible to obtain negative protection command as follows:

$$u_p^-(t) = -r(t)e^{-\eta(x_1(t) - X_{lim} + \xi x_2(t))} \tag{41}$$

2. Offline Parametric Study on Tuning

This section presents a short study on the effect of tuning variables η and ξ. For brevity, the analysis focuses on bank angle protection, the limits and mechanism of which are outlined in the next subsection. The parametric study is carried out by systematically varying each parameter individually while holding the other at a constant value of 1. For all simulations in this section, a roll rate input of 10 deg/s is applied for a duration of 20 seconds between t = 10 and 30. Figure 5 presents the results of this study. Judging from Figure 5a, increasing η while keeping ξ constant reduces the

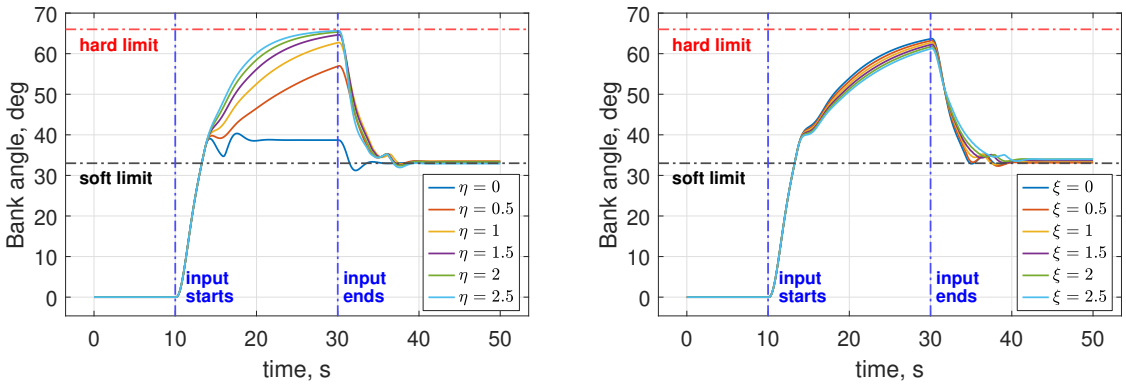

(a) Variable η with $\xi = 1$ **(b) Variable ξ with $\eta = 1$**

Fig. 5 Results of the parametric study

damping of the response. As η decreases, the correction from the FEP becomes more severe. This is evidenced by the slight oscillation at approximately t = 13 seconds, which is expected since bank protection only starts to act after the aircraft exceeds the soft limit. The oscillation is barely noticeable at $\eta = 2.5$, but becomes increasingly pronounced at lower values. In addition, aggressive correction at lower η values prevents the bank angle from reaching the hard limit while the roll rate input is active. From Figure 5b, it is possible to notice that compared to η, changing ξ has less impact on the initial part of the response until t = 30 s. Higher ξ values lead to a slightly more damped response. At lower ξ values, the response is closer to the hard limit, and it moves further away at higher values. An interesting result of changing ξ is observed during the aircraft's return to the soft limit. Although the oscillation before settling remains for all values, at higher values, the return occurs more slowly and smoothly. This potentially has vehicle-specific implications on passenger comfort for commercial aircraft. Further details on stability proofs and tuning are available in [40, 41].

3. Application to Flying V FEP System

With the theoretical derivation complete, the next step involves extending this approach to the Flying V FEP system. Table 4 provides a summary of Flying V FEP limits and protection mechanisms, drawing on industry methodologies used by Airbus and Boeing [17, 26]. Bank protection limits the state while commanding its rate. Therefore, its FEP can

Table 4 FEP overview

Protected state	Limits	Protection mechanism
Angle of attack, α	pitch break dependent	scale down maximum load factor limit, $n_{z,max}$
Bank angle, ϕ	$\phi_{s,lim} = \pm 33°$:soft limit $\phi_{h,lim} = \pm 67°$:hard limit	limit pilot roll rate input, $\dot{\phi}_{com}$, inactive when $\phi < 33°$ if $\phi > 33°$ and stick released, $\phi_{h,lim} = 33°$
Load factor, n_z	$n_{z,min} = -1$:nose down $n_{z,max} = 2.5$:nose up	limit $n_{z,com}$, given in Eq. (25)
Pitch, θ	$\theta_{min} = -15°$:nose down $\theta_{max} = 30°$:nose up	limit $\dot{\theta}_{com}$, given in Eq. (27)

be directly implemented by limiting pilot roll rate inputs. On the other hand, angle of attack, load factor, and pitch are

more involved since the pilot pitch channel command is a C*U parameter. As explained in subsection III.E, the C*U parameter must be reformulated into the commanded load factor and pitch rate, given respectively in Eqs. (25) and (27).

Adhering to the formulation given in Eqs. (39) and (41), the bank protection is given as

$$\dot{\phi}_p = \max\left(\dot{\phi}_{com} e^{-\eta_\phi(\phi-\phi_{min}+\xi_\phi\dot{\phi}_m)}, \min\left(\dot{\phi}_{com}, \dot{\phi}_{com} e^{\eta_\phi(\phi-\phi_{max}+\xi_\phi\dot{\phi}_m)}\right)\right) \tag{42}$$

In this expression, ϕ_{max} and ϕ_{min} represent the positive and negative ends of the limits. They are defined by the soft limits during wings-level flight and switch to hard limits when the pilot commands lateral stick inputs. Similarly, the pitch protection is written as follows:

$$\dot{\theta}_p = \max\left(\dot{\theta}_{com} e^{-\eta_\theta(\theta-\theta_{min}+\xi_\theta\dot{\theta}_m)}, \min\left(\dot{\theta}_{com}, \dot{\theta}_{com} e^{\eta_\theta(\theta-\theta_{max}+\xi_\theta\dot{\theta}_m)}\right)\right) \tag{43}$$

As outlined in Table 4, the angle of attack protection functions by scaling down the maximum load factor limit, $n_{z,max} = 2.5$. This works because the load factor and angle of attack are related through the lift coefficient. Following similar logic, a limiting command can be formulated for $\dot{\alpha}$. Since the goal is to limit the commanded load factor, the protection command should be multiplied by a gain K_α. This gain is a design parameter that scales $\dot{\alpha}$ with $n_{z,com}$. In this research, K_α is set to 1. However, this parameter may necessitate more precise tuning when accounting for vertical gust loads or when applied to highly agile aircraft. Based on this, α-constrained load factor is given in Eq. (44).

$$n^{\alpha}_{z,p} = n_{z,com} K_\alpha e^{\eta_\alpha(\alpha-\alpha_{max}+\xi_\alpha\dot{\alpha}_m)} \tag{44}$$

where α_{max} is determined in flight based on the angle of attack at which pitch break occurs. The aerodynamic model described in Table 1 is available in multiple flight conditions. In each flight condition, the pitch break AoA is retrieved from the C_{M_α} curve of the aerodynamic model. Then the angle of attack limit is calculated by dynamically interpolating between flight conditions using indicated airspeed. The load factor protection is the final component of the FEP. Load factor essentially represents acceleration; thus determining the limiting command via potential functions requires knowing its rate, which corresponds to vertical jerk. Instead, we can assume that the damping element ξ_{n_z} is zero, leading to:

$$n^{+}_{z,p} = n_{z,m} e^{\eta_{n_z}(n_{z,m}-n_{z,max})}, \quad n^{-}_{z,p} = n_{z,m} e^{-\eta_{n_z}(n_{z,m}-n_{z,min})} \tag{45}$$

Following this, the final protection that combines angle of attack and load factor is expressed as

$$n_{z,p} = \max\left(-1,\ n^{-}_{z,p},\ \min\left(2.5,\ n_{z,com},\ n^{\alpha}_{z,p},\ n^{+}_{z,p}\right)\right) \tag{46}$$

One key distinction between angle of attack and load factor protection is that the former constrains the commanded load factor $n_{z,com}$ to safeguard α, whereas the latter restricts the measured load factor $n_{z,m}$ to prevent structural overstress by ensuring compliance with the hard load factor limits specified in Table 4.

This concludes the discussion on the FEP as well as the normal flight law. The next section tackles the problem of outer loop gain tuning using multi-objective optimization.

IV. Multi-Objective Parameter Optimization for Gain Tuning

The performance of the normal flight law depends strongly on the outer loop control gains. Therefore, the selection of these gains constitutes an important component of flight control design. In pursuit of this goal, we utilize a multi-objective optimization approach that includes both handling quality criteria for linear systems and requirements for nonlinear transient behavior. The aim is to tune the outer loop to deliver Level 1 handling qualities based on a linearized system while maintaining satisfactory transient response characteristics in the nonlinear system. Table 5 provides an overview of the optimization objectives. The optimization is performed separately for longitudinal and coupled lateral-directional channels, which represents a reasonable approach as pitch commands do not excite roll and yaw dynamics. Conversely, roll and yaw channels remain inherently coupled primarily due to the Dutch roll mode.

Linear constraints originate from the military standard 1797A [58] for terminal and non-terminal flight phases under the assumption that the Flying V is a Class III aircraft. This standard outlines satisfactory (Level 1), acceptable (Level 2), and controllable (Level 3) response characteristics for linearized systems. Given the nonlinear nature of the Flying V simulation model, it must be linearized before enforcing any constraints. However, it is not straightforward to obtain a linearized system matrix with distinct dynamic modes for the normal law. With the advent of fly-by-wire controls, the

Table 5 Constraints overview

Linear			
Constraint type	Constraint	Constraint value	Dynamics
Gain margin, dB	GM_p, GM_q, GM_r	$GM \geq 6$	All
Phase margin, deg	PM_p, PM_q, PM_r	$PM \geq 45$	All
Frequency, rad/s	ω_{sp}, ω_{dr}	$\omega_{sp} \geq 1$, $\omega_{dr} \geq 0.5$	All
Damping ratio	ζ_{sp}, ζ_{dr}	$1.3 \geq \zeta_{sp} \geq 0.35$, $\zeta_{dr} \geq 0.08$	All
Frequency-damping product, rad/s	$\omega_{dr}\zeta_{dr}$	$\omega_{dr}\zeta_{dr} \geq 0.15$	Roll-yaw
CAP, $g^{-1}s^{-2}$	$\omega_{sp}^2/(V/gT_{\theta,2})$	$3.6 \geq CAP \geq 0.085$	Pitch
Bandwidth, rad/s	$\omega_{\theta,bw}$	$\omega_{\theta,bw} \geq 3$	Pitch
Delay parameter, s	τ_p	$0.1 \geq \tau_p \geq 0$	Pitch-roll
Time constant, s	T_s, T_r	$17.3 \geq T_s \geq 0$, $1 \geq T_r \geq 0$	Roll-yaw
Nonlinear Transient Response			
Input type	Minimization constraints	Constraint value	Dynamics
Step $\Delta(C^*U)_{com} = 0.5$	OS (-), ST (s), CE (deg)	—	Pitch
Step $\dot{\phi}_{com} = 3$ deg/s	OS (deg/s), ST (s), CE (deg)	—	Roll
Step $\beta_{com} = 5$ deg	OS (deg), ST (s), CE (deg)	—	Yaw

number of system states grew significantly for aircraft. The additional dynamics introduced by the control laws makes it difficult to isolate and identify the frequency of each dynamic mode. A recognized method for solving this problem is the equivalent systems principle. This method extracts an input-output transfer function from the complete linear model. The frequency response is then matched to that of a reduced lower-order system in the 0.1 to 10 rad/s range, with this system characterizing a distinct dynamic mode. For longitudinal dynamics, [58] suggests simultaneously fitting a pitch rate and load factor lower-order equivalent system (LOES) to the higher-order system (HOS). These transfer functions are given and explained in [59]. To linearize the system and derive higher-order systems, this study employs a block-by-block linearization methodology using the Matlab/Simulink Control Systems Toolbox. This approach separates the system components into tunable and static blocks. Since static blocks are constant, they are linearized only once. For tunable blocks, the process involves generating a list of normally distributed gains, linearizing each block individually, integrating them with the static system, and extracting linear parameters across all gain configurations. The gain and phase margins are calculated by opening the feedback loop right before the INDI block in Figure 2 and performing a loop transfer. Lastly, $\omega_{\theta,bw}$ is the pitch attitude bandwidth and the delay parameter $\tau_p = -(\phi_{2,\omega_{180}} + 180°)/(57.3 \times 2\omega_{180})$. In this expression, ω_{180} is the frequency at -180 degree phase angle, whereas $\phi_{2,\omega_{180}}$ is the phase angle at $2 \times \omega_{180}$.

The nonlinear constraints focus on the transient response of the system to step inputs along each control channel. These constraints include overshoot (OS), settling time (ST), and control effort (CE). Overshoot and settling time are well-known transient response characteristics. On the other hand, the control effort is calculated by continuously summing all control surface deflections and normalizing by the total flight/simulation time. Minimizing the nonlinear constraints while satisfying the linear ones ensures that the system maintains desirable handling qualities and retains good tracking performance.

Once both linear and nonlinear simulations are complete for all gain configurations, a score is assigned to each based on the linear and nonlinear performance constraints given in Table 5. The configuration with the best score is then selected, and a second gain list is uniformly generated around this configuration. This process is performed using an automated interior-point optimization algorithm implemented through the fmincon function in MATLAB. The optimization stops when the score does not improve for two consecutive iterations. The gain configuration refers to specific values for each tunable parameter, while a gain list is an array of gains for each parameter.

V. Experimental Design

The experiment is designed to evaluate the handling qualities of normal flight law, validate the flight control system design, and assess flight envelope protection capabilities. Based on the design covered in the preceding sections, it is possible to derive several hypotheses about the outcome of the experiment. First, since the outer loop controllers are tuned to provide satisfactory transient response and Level 1 handling qualities, pilot ratings and verbal feedback should accordingly reflect Level 1 performance. Second, the angle of attack protection should prevent pitch break for all maneuvers and across all flight conditions. Given that the FEP is based on exponential potential functions, this should happen smoothly and without significant interference with pilot commands during normal operation. Similarly, roll/bank angle protection should successfully introduce soft and hard limits and prevent excessive bank angles. Lastly, considering that the outer loop control architecture is industry-inspired, general control and handling of the aircraft should feel natural and intuitive to the pilots. The autothrottle remains active for the entire experiment. If desired, pilots can select different autothrottle reference speeds using the mode control panel.

A. Maneuvers and Flight Conditions

The experiment includes three categories of maneuvers: all-engines operative (AEO), one-engine-inoperative (OEI), and flight envelope protection. In addition, five flight conditions are chosen based on available aerodynamic data to reflect critical flight phases, such as take-off, landing, and cruise. AEO and OEI maneuvers are carried out in all flight conditions, whereas the FEP maneuvers are carried out only in a single flight condition.

The maneuvers originate primarily from EASA's initial CS-25 airworthiness specifications [44]. With the exception of pitch tracking, AoA protection, and roll protection. Pitch tracking maneuver is evaluated using the Cooper-Harper Rating Scale [60] in relation to the desired and adequate performance requirements. On the other hand, AoA and roll protection maneuvers are developed to test these functionalities of the flight envelope protection. Table 6 provides the complete list of manuvers, their definitions, performance margins, and driving requirements. Maneuvers based on CS-25 are relevant in terms of certification. On the other hand, subjective tasks like pitch tracking allow extracting handling qualities and facilitate discussion between the pilots carrying out the maneuvers and the control designers. Table 7 provides an overview of all flight conditions. All of these conditions are evaluated at the aft CG. Considering the pitch break tendencies of the Flying V, the aft CG represents the worst possible condition in terms of longitudinal stability. At lower speeds, the high lift devices (HLDs) are deflected to reduce the angle of attack necessary to trim the aircraft. This increases the margin to pitch break, which indirectly improves control effectiveness. According to [6], deploying high lift devices can boost the effectiveness of primary control surfaces by up to 40%. During the experiment, these devices are static, which means that the pilot does not have control over them, and they remain deployed for all low-speed maneuvers. At cruise speeds, HLDs are not deflected, as this would require unrealistic hinge moments and introduce excessive drag.

B. Apparatus

The experiment is carried out in the SIMONA Research Simulator (SRS) of Delft University of Technology [42]. SRS is a hydraulic-powered 6-DOF moving-base flight simulator that has been operational since the early 2000s. The simulator consists of configurable flight deck, realistic control loading, tuneable motion cues, and collimated outside visuals. A middleware called Delft University Environment for Communication and Activation (DUECA) regulates synchronization, communication, and scheduling between different subsystems [61]. Figure 6 shows the interior and exterior of the SRS as configured for the experiment. A detailed description of the flight deck instruments, control loading system, and motion system are available in [59].

1. Flight Deck Instruments

The SRS features a configurable two-person flight deck, comparable to standard commercial aircraft cockpits. The simulator provides flexible control options like control column, sidestick, center stick, and steering wheel, adaptable to specific simulation goals. In addition, the hardware includes programmable touchscreens, head-up and primary flight displays, a replica of the B737 mode control panel, and an original B777 control pedestal. The outside view is a collimated 180 by 40 degree visual supported by three LED-based DLP projectors. By default, the left pilot seat is fitted with a control column and pedals, while the right seat includes a sidestick with an armrest and pedals. This study uses the right seat configuration.

In addition to the outside visual, the pilot can use a custom flight display on the main instrument panel in front

of them. The symbology on this display is based on that of a Head-Up Display (HUD), as seen in Figure 6b. The mostly green on black background symbology provides the most important flight parameters, as well as task-specific information such as tracking targets, margins, and indicators of control surface saturation.

Table 6 Flight maneuvers and requirements

Maneuver	Description	Margins	Driving Req.
Pitch tracking (PT)	Follow a pitch reference signal made up of constants, ramps, and sinusoids for X[††] percentage of time	Adequate: ±1° Desired: ±0.5°	—
Coordinated turn (CT)	Capture a 40° bank angle, perform a coordinated turn for 10 seconds	FPA: 0° and 5° IAS: ±5%, kts Sideslip: ±2°	CS 25.143(h)
Bank-to-bank (BTB)	Capture a 30° bank angle, ensure turn coordination, reverse to -30° under 7 seconds	FPA: 0° and 5° IAS: ±5%,kts	AMC 25.147(f)
Steady-heading sideslip (SHS)	Capture a desired sideslip that depends on flight condition, maintain steady heading for 10 seconds	FPA: 0° and 5° Heading: ±5° Sideslip: ±2°	AMC 25.177(c)
Coordinated turn (OEI)	Capture a 20° bank angle, perform coordinated turn for 10 seconds, reverse to a -20° coordinated turn, maintain for 10 seconds	FPA: 0° and 5° IAS: ±5%, kts Sideslip: ±2 °	CS 25.147(c)
Bank-to-bank (OEI)	Same as nominal BTB, but under 11 seconds	FPA: 0° and 5° IAS: ±5% Sideslip: ±2 °	AMC 25.147(d)
Dynamic sideslip (OEI)	Capture a 7.5° sideslip while keeping steady heading, reverse to -7.5° sideslip under 7 seconds	FPA: 0° and 5° IAS: ±5%, kts	CS 25.147(a)
AoA protection	Set engines to idle by choosing a low reference speed using the mode control panel, aircraft will try to descent, slowly increase stick inputs to pull up, continue until the rate of descent comes to a stop	FPA: -10° and 5°	—
Roll protection	Apply full lateral stick deflection, aircraft will start descent, once inside margins, continue full stick for another 10 seconds, release the stick completely	FPA: -20° and 0° Bank: 45 to 66°	—

Table 7 Flight conditions

Condition	IAS, kts	Altitude, ft	Weight, t	HLD, deg
Approach 1	132.3	0	MLW	40
Approach 2	165.4	0	MLW	30
Take-off	198.5	0	MTOW	30
Cruise 1	241.3	25098	MTOW	-
Cruise 2	261.0	36827	MTOW	-

[††]X depends on flight condition

(a) SRS from the outside **(b) SRS from the inside**

Fig. 6 SIMONA Research Simulator

2. Control Loading System

The control loading system essentially emulates the feel of real aircraft by providing realistic force feedback on pilot inputs. Since the Flying V is in the early design stages, choosing appropriate control forces is not straightforward. This study employs a control configuration similar to Airbus aircraft, utilizing sidestick inputs for pitch and roll channels and pedals for yaw control. Thus, control forces are determined using existing Airbus references. The exact characteristics of the sidestick and the pedals are given in [59]. Proper selection of these parameters is important for realistic flight simulation because improper choices may increase pilot-induced oscillation (PIO) tendencies and artificially reduce pilot ratings.

3. Motion System

The motion base of the SRS consists of six hydraulic actuators with an operating pressure of 160 bar and a stroke of 1.15 meters [42]. The pressure of individual actuators is regulated by a comprehensive control algorithm that accounts for the inertial and dynamic properties of the simulator, as well as the reference motion from the motion cueing filters. The motion cues are tuneable and contribute to a realistic flight simulation. Motion cueing settings used in this study are given in [59]. During the experiment, the motion system remained active only for all-engines operative maneuvers. The FEP and one-engine-operative maneuvers are conducted without motion due to their potentially high acceleration nature.

C. Participants

Pilot feedback plays an important role for the Flying V. Given the iterative and dynamic nature of ongoing developments, pilot evaluations enable flight control engineers to identify design limitations and refinement opportunities. In this study, two technical airline pilots participated in simulated flight tests for evaluation. Although it may seem like a small number, it is important to note that technical pilots are different from regular line pilots. They are not only captain level pilots, but also possess advanced knowledge on flight operations, certification, and flight testing. One pilot serves as a captain for Boeing planes, while the other is for Airbus. This provides a unique opportunity to evaluate our industry-inspired flight controller and gather expert opinion.

VI. Results and Discussion

This section presents the experiment results and provides a detailed discussion. The results are categorized into handling qualities, CS-25 certification maneuvers, flight envelope protection maneuvers, and pilot feedback.

A. Handling Quality Ratings

The handling qualities are assessed for the pitch tracking task using the Cooper-Harper Rating Scale (CHRS) and verbal pilot feedback. During the maneuver, pilots accumulate desired and adequate scores based on the time spent inside the margins as a percentage of the total tracking time. The target for both scores are communicated to the pilots before the experiment. Pilots are required to adjust their input gain to maintain the scores. This process helps in

revealing any undesirable characteristics of the aircraft and enables pilots to provide a rating according to desired and adequate mission performance. Figure 7 shows the ratings in all flight conditions for both pilots. Evidently, pilots rated

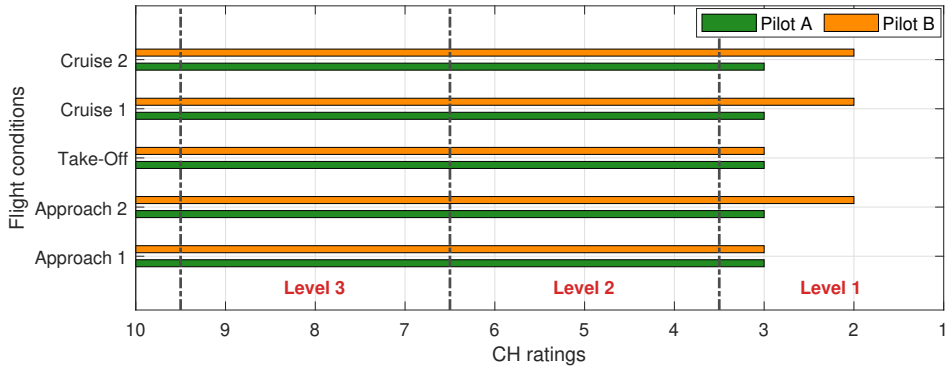

Fig. 7 Cooper-Harper ratings across flight conditions for pitch tracking (PT)

most conditions as 3 on the CHRS, with pilot B rating some as 2. A rating of 2 means that pilot compensation is not a factor in achieving desired performance, whereas 3 indicates minimal pilot compensation for desired performance. According to military standard 1797A [58], a CH rating of 1 to 3 corresponds to Level 1, a rating between 4 and 6 signifies Level 2, and a rating from 7 to 9 indicates Level 3. Hence, with the control architecture proposed in this paper, the Flying V exhibits Level 1 handling qualities, fulfilling the normal law goals established in Section III. The absence of variation in ratings arises because the outer loop controllers are tuned in each flight condition to ensure Level 1 handling qualities, as detailed in Section IV. Consequently, the controller augments the Flying V to maintain desired performance across all flight conditions.

Regarding verbal feedback, some of the pilot statements include the following. The pitch rate damping is less compared to real aircraft but similar to other flight simulators. Aiming for the desired score results in load factors between 0.7 and 1.3, which is overly aggressive for passenger flights and resembles certification flights. The tracking signals are followable but demanding, which deteriorates CH ratings. For a more gentle flight with passengers, the ratings would be closer to 1. Capturing pitch angles requires stick inputs for a longer duration compared to real aircraft, negatively impacting the ratings. Lastly, the stick force along the pitch channel is slightly larger compared to Airbus aircraft.

For pitch tracking tasks, the speed stability element of the C*U controller is disabled, meaning that it behaves as a conventional C* controller. During pre-testing, the speed stability component was found to reduce predictability in pitch tracking tasks. This occurs when the pitch target changes rapidly. For example, in response to an increase in pitch target, the pilot commands nose-up input, which consequently reduces aircraft speed momentarily. The speed stability mechanism then initiates nose-down to recover airspeed before the engines can react and stabilize speed.

B. Certification Maneuver Results

The certification maneuvers originate from EASA CS-25 initial airworthiness specifications and are evaluated on a pass/fail basis. Based on Table 6, these maneuvers are classified into two as all-engines-operative and one-engine-inoperative. The maneuvers include coordinated turns, time to bank, as well as steady and dynamic sideslip requirements. The nature of the maneuvers differ depending on the engine setting. Tables 8 and 9 provide the results of the maneuvers across all flight conditions performed by both pilots.

Starting with Pilot A, almost all maneuvers are successful, excluding coordinated turn under two flight conditions. The maneuver failed at Cruise 1 due to a combination of pitch and roll oscillations introduced by the AoA and bank protections. This flight condition is particularly close to pitch break, which leaves little margin for pulling up during turns. Despite full aft stick deflection, pilot could not exceed the AoA limit of 7 degrees. Since bank protection is active during the maneuver, the pilot is required to apply a lateral stick while coordinating the turn. The absence of force feedback on the sidestick for bank protection created additional difficulty in selecting and maintaining a bank angle. Similarly, in Approach 1, capturing the target bank of 40-45° brings the aircraft to the verge of pitch break, where interference from AoA protection prevents the pilot from stabilizing the flight path angle. The results are similar for Pilot B, where the coordinated turn in Cruise 1 failed due to the same reason. However, Pilot B successfully coordinated the turn in Approach 1 by positioning the aircraft at a high pitch attitude before initiating the turn.

Table 8 Results of certification maneuvers (Pilot A)

FC	CT	BTB, s	SHS	CT-OEI	BTB-OEI, s	DSS-OEI, s
Approach 1	Fail	Pass (6.1)	Pass	Pass	Pass (8.0)	Pass (6.8)
Approach 2	Pass	Pass (5.8)	Pass	Pass	Pass (8.0)	Pass (7.0)
Take-Off	Pass	Pass (3.4)	Pass	Pass	Pass (-)	Pass (6.0)
Cruise 1	Fail	Pass (3.7)	Pass	Pass	Pass (5.9)	Pass (6.7)
Cruise 2	Pass	Pass (5.9)	Pass	Pass	Pass (5.4)	Pass (4.5)

Table 9 Results of certification maneuvers (Pilot B)

FC	CT	BTB, s	SHS	CT-OEI	BTB-OEI, s	DSS-OEI, s
Approach 1	Pass	Pass (3.4)	Pass	Pass	Pass (4.5)	Pass (5.3)
Approach 2	Pass	Pass (3.5)	Pass	Pass	Pass (4.3)	Pass (2.7)
Take-Off	Pass	Pass (4.8)	Pass	Pass	Pass (5.0)	Pass (2.4)
Cruise 1	Fail	Pass (3.6)	Pass	Pass	Pass (3.9)	Pass (4.2)
Cruise 2	Pass	Pass (4.5)	Pass	Pass	Pass (4.1)	Pass (2.5)

In general, the pilots reported that the aircraft behaves smoothly with well-damped responses and is pleasant to fly. They found it comparable to real aircraft that no rudder compensation is necessary after engine failure and praised the lack of roll compensation needed to maintain a steady heading in sideslip flight. In most cases, they could perform the steady-heading sideslip maneuver without using the sidestick. However, the pilots identified two issues. First, the AoA protection system generated unwanted pitch oscillations, which can be seen in the AoA plot of Figure 8 after 50 s. These oscillations likely stem from the chattering behavior explained in the following subsection. Second, turn coordination at low speeds required higher rudder inputs compared to similar class Boeing and Airbus aircraft. This indicates that the tuning of some lateral-directional gains requires further investigation, as no control surface saturation was observed during these maneuvers.

C. Flight Envelope Protection Results

Referring back to Table 6, the FEP maneuvers focus on angle of attack and bank protection. The former is particularly important for the Flying V due to its pitch break tendencies. For the AoA maneuver, starting from a wings-level trimmed flight condition, the pilot is asked to choose a very low target speed for the autothrottle, which essentially sets the engines to idle. The pilot is then asked to maintain pitch attitude by applying increasing longitudinal stick deflections. This causes AoA to increase steadily as the velocity drops. The goal of the maneuver is to validate that the AoA protection system, which uses exponential potential functions, effectively prevents pitch break. Figure 8 outlines the results of this maneuver based on Pilot A's simulation run in Cruise 1 flight condition. Starting with the top right subfigure, the pilot slowly increases their $\Delta(C^*U)$ input via longitudinal stick commands, while trying to keep their lateral roll rate inputs under control. Around 55 seconds after the run starts, the pilot starts to command full stick deflection, which corresponds to a $\Delta(C^*U)$ input of 2. Switching to the AoA plot on the upper left subfigure, despite a full deflection command for over 100 seconds, the AoA follows the limit with a respectable buffer and does not oscillate over the limit. This characteristic of AoA protection is significantly different compared to conventional commercial aircraft. Typically, AoA protections function by forcibly pushing the nose of the aircraft down, when the AoA approaches critical values. However, the critical AoA values are quite low in flying wings compared to conventional aircraft. As a result, the aggressive method of pushing the nose down is highly likely to interfere with standard flight phases. Instead, the approach presented in this paper limits the AoA in a safe and smooth way with minimal interference. For example, although the AoA is limited, the aircraft can still climb. Furthermore, by tuning the design parameters ξ_α, η_α, and K_α, the buffer to the limits can be adjusted to account for sudden disturbances such as vertical gusts that might push the AoA over the limit. Finally, looking at the lower figures, the roll oscillations and the resulting yaw are caused by accidental lateral pilot inputs, while pitch follows the AoA after t = 50 seconds, indicating a steady flight path angle. The downside

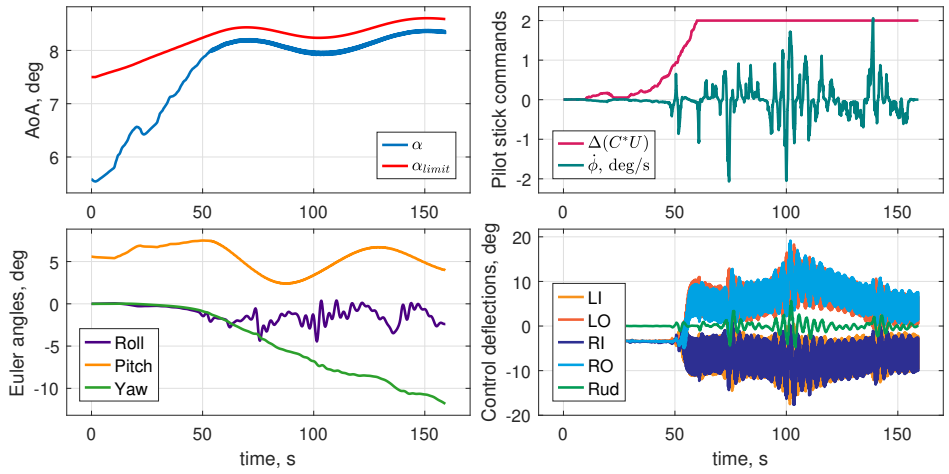

Fig. 8 Angle of attack protection maneuver (Pilot A, Cruise 1)

to this approach is the increase in control effort, as seen in the lower right figure. During the experiment, the elevons started to intermittently saturate their rate limit, and chatter. The upside is that the surfaces never hit their deflection limits, leaving control authority to further steer the aircraft.

The second FEP maneuver is for bank or roll protection. In this, starting from a wings-level trimmed flight condition, the pilot applies full lateral stick deflection without pulling up, which causes the aircraft to slowly start descending. When the flight path angle drops below zero, a timer is activated for 10 seconds. After this duration, the pilot fully releases the sidestick. The goal of the descent is to avoid longitudinal envelope protections, allowing for a distinct evaluation of the roll protection. Figure 9 illustrates the results of this maneuver carried out by Pilot B in Cruise 2 flight condition. Starting with the upper right figure, during the first 10 seconds of the maneuver, the pilot applies full lateral

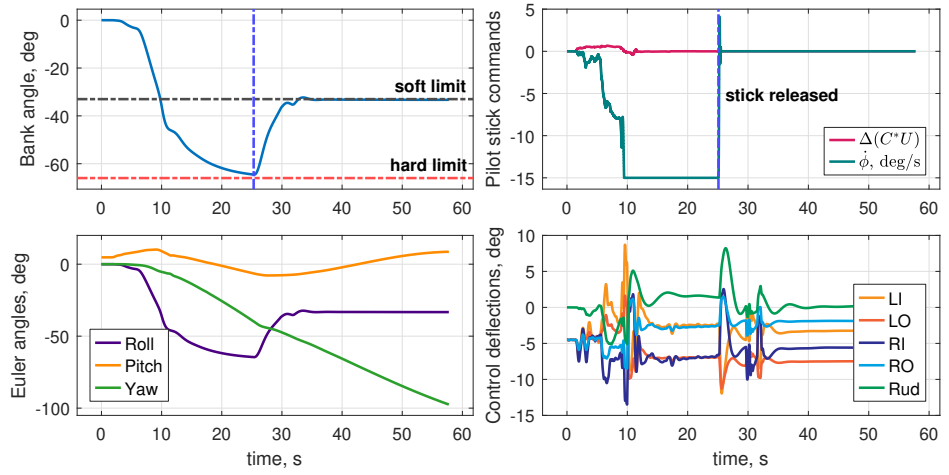

Fig. 9 Bank protection maneuver (Pilot B, Cruise 2)

stick, which corresponds to a roll rate of -15 deg/s, as well as some unintentional longitudinal inputs. The pilot maintains maximum deflection for around 15 seconds and releases the stick abruptly. The consequence of this on the bank angle is visible in the upper left figure. Since the bank protection is inactive below the soft limit, the initial response is sharp. However, after the bank crosses the soft limit, the protection becomes active and starts to dampen out the response. This is visible from the small oscillation around t = 12 seconds. Between the soft and hard limits, the response essentially is an exponential function approaching its limit. Once the stick is released, the bank returns back to its soft limit with another exponential function, while exhibiting some small oscillations before settling. Based on the FEP overview given in Table 4, this behavior matches well with the FEP design, except for the slight oscillations. Furthermore, the pilots

noted that the bank protection feels comparable to real aircraft. Judging from the attitude angles in the bottom left figure, it is evident that the pitch angle also recovers once the bank returns to its soft limit. This recovery is achieved due to the C*U controller and the pitch compensation element. Finally, the control deflections plotted in the bottom right corner do not display deflection saturation, leaving control authority for further maneuverability.

VII. Conclusions

Flying wing designs might hold the key to improving fuel efficiency in commercial aviation. However, they raise concerns due to their limited lateral-directional damping and longitudinal instability tendencies at high angles of attack. Consequently, fly-by-wire flight control becomes an essential factor for the commercialization of flying wings.

This paper improves the existing flight control laws of a commercial flying wing aircraft design called the Flying V, presents industry-inspired flight control laws, and conducts piloted flight simulations to evaluate these laws. Evaluation includes maneuvers to assess handling qualities, certification compliance, and flight envelope protection (FEP) capabilities. The control laws use a cascaded structure with an outer loop that combines Airbus and Boeing design philosophies, along with angle of attack, bank, pitch, and load factor protections. The FEP employs command limiting exponential potential functions, which smoothly enforces envelope limits, prevents overshoots, and ensures minimal interference during nominal flight phases. The inner inversion loop is based on incremental nonlinear dynamic inversion.

The results show that the Flying V model, augmented with the proposed normal law flight controls, delivers Level 1 handling qualities and satisfies nearly all chosen certification requirements. The FEP successfully enforces limits and prevents longitudinal instability, i.e., pitch break, despite deliberate attempts by pilots to stall the aircraft. The angle of attack protection does not aggressively force pitch-down movement and allows for maneuverability even close to pitch break. The bank protection successfully enforces soft and hard limits, displaying performance similar to real aircraft as noted by the pilots. This underlines the strong capabilities of command limiting exponential potential functions for flight envelope protection design.

Although the controller delivers satisfactory overall performance, the experiments reveal some limitations. When operating in flight conditions close to stall or pitch break, the margin to pull up is limited. As a result, putting the nose up and initiating turns quickly activates the angle of attack protection, which introduces small pitch oscillations. Even though the root cause of this is the pitch break limitations of the Flying V, the oscillatory nature of the protection warrants further investigation. In addition, pilots noticed that turn coordination at lower speeds necessitates slight rudder compensation, which is unexpected for normal flight laws. Hence, coordination capabilities of the control laws at low speed require further study. Furthermore, future research should investigate atmospheric disturbances such as gusts and their impact on the FEP.

Commercializing flying wings is a challenging problem to solve solely using flight controls. Further studies should involve the joint effort of aerodynamics experts, aircraft designers, and control engineers to improve the airframe alongside the controller.

Acknowledgments

This publication is part of the project Flying V Flight Control with project number 19511 of the Open Technology Program, which is (partly) financed by the Dutch Research Council (NWO). The authors would like to acknowledge the in-kind contributions to the project of KLM Royal Dutch Airlines and ADSE Consulting and Engineering.

References

[1] Martínez-Val, R., Cuerno, C., Pérez, E., and Ghigliazza, H. H., "Potential Effects of Blended Wing Bodies on the Air Transportation System," *Journal of Aircraft*, Vol. 47, No. 5, 2010, pp. 1599–1604. https://doi.org/10.2514/1.C000214.

[2] Benad, J., and Vos, R., "Design of a Flying V Subsonic Transport," *33rd Congress of the International Council of the Aeronautical Sciences*, ICAS Paper 2022-0358, Sep. 2022. URL https://www.icas.org/ICAS_ARCHIVE/ICAS2022/data/preview/ICAS2022_0358.htm.

[3] Bolsunovsky, A. L., Buzoverya, N. P., Gurevich, B. I., Denisov, V. E., Dunaevsky, A. I., Shkadov, L. M., Sonin, O. V., Udzhuhu, A. J., and Zhurihin, J. P., "Flying Wing - Problems and Decisions," *Aircraft Design*, Vol. 4, No. 4, 2001, pp. 193–219. https://doi.org/10.1016/S1369-8869(01)00005-2.

[4] Asaro, S., and Vos, R., "Synthesis of the Aerodynamic Model of a Flying Wing Aircraft," *AIAA SciTech Forum*, AIAA Paper 2025-0852, Jan. 2025. https://doi.org/10.2514/6.2025-0852.

[5] Palermo, M., and Vos, R., "Experimental Aerodynamic Analysis of a 4.6%-Scale Flying-V Subsonic Transport," *AIAA SciTech Forum*, AIAA Paper 2020-2228, Jan. 2020. https://doi.org/10.2514/6.2020-2228.

[6] Asaro, S., Atmaca, D., van Kampen, E., and Vos, R., "Control Surface Allocation Based on Offline Handling Quality Simulations for a Flying Wing Aircraft," *CEAS Aeronautical Journal*, Oct. 2025. https://doi.org/10.1007/s13272-025-00906-2.

[7] Stougie, J., Pollack, T., and van Kampen, E., "Incremental Nonlinear Dynamic Inversion Control with Flight Envelope Protection for the Flying-V," *AIAA SciTech Forum*, AIAA Paper 2024-2565, Jan. 2024. https://doi.org/10.2514/6.2024-2565.

[8] Atmaca, D., Stroosma, O., and van Kampen, E., "Piloted Evaluation of Flying-V with Incremental Nonlinear Dynamic Inversion and Envelope Protection," *AIAA SciTech Forum*, AIAA Paper 2025-0973, Jan. 2025. https://doi.org/10.2514/6.2025-0973.

[9] van Overeem, S., Wang, X., and van Kampen, E., "Handling Quality Improvements for the Flying-V Aircraft using Incremental Nonlinear Dynamic Inversion," *AIAA SciTech Forum*, AIAA Paper 2023-0105, Jan. 2023. https://doi.org/10.2514/6.2023-0105.

[10] Garcia, A. R., Brown, M., Atherstone, D., van Arnhem, N., and Vos, R., "Aerodynamic Model Identification of the Flying V from Sub-Scale Flight Test Data," *AIAA SciTech Forum*, AIAA Paper 2022-0713, Jan. 2022. https://doi.org/10.2514/6.2022-0713.

[11] Garcia, A. R., Vos, R., and de Visser, C., "Aerodynamic Model Identification of the Flying V from Wind Tunnel Data," *AIAA SciTech Forum*, AIAA Paper 2020-2739, Jun. 2020. https://doi.org/10.2514/6.2020-2739.

[12] Joosten, S., Stroosma, O., Vos, R., and Mulder, M., "Simulator Assessment of the Lateral-Directional Handling Qualities of the Flying-V," *AIAA SciTech Forum*, AIAA Paper 2023-0906, Jan. 2023. https://doi.org/10.2514/6.2023-0906.

[13] van Overeem, S., Wang, X., and van Kampen, E., "Modelling and Handling Quality Assessment of the Flying-V Aircraft," *AIAA SciTech Forum*, AIAA Paper 2022-1429, Jan. 2022. https://doi.org/10.2514/6.2022-1429.

[14] Traas, T., Atmaca, D., and van Kampen, E., "Hybrid Incremental Nonlinear Dynamic Inversion Control with Flight Envelope Protection for Flying Wing Aircraft," *AIAA SciTech Forum*, Jan. 2026.

[15] Atmaca, D., and van Kampen, E., "Fault Tolerant Control for the Flying-V Using Adaptive Incremental Nonlinear Dynamic Inversion," *AIAA SciTech Forum*, AIAA Paper 2025-0081, Jan. 2025. https://doi.org/10.2514/6.2025-0081.

[16] Lombaerts, T., Looye, G., Ellerbroek, J., and y Martin, M. R., "Design and Piloted Simulator Evaluation of Adaptive Safe Flight Envelope Protection Algorithm," *Journal of Guidance, Control, and Dynamics*, Vol. 40, No. 8, 2017, pp. 1902–1924. https://doi.org/10.2514/1.G002525.

[17] Bartley, G. F., "Boeing B-777: Fly-By-Wire Flight Controls," *The Avionics Handbook*, CRC Press LLC, Williamsburg, VA, 2001, 1st ed.

[18] Niedermeier, D., and Lambregts, A. A., "Fly-By-Wire Augmented Manual Control - Basic Design Considerations," *28th International Congress of the Aeronautical Sciences*, ICAS Paper 2012-5.4.1, Sep. 2012. URL https://www.icas.org/icas_archive/ICAS2012/ABSTRACTS/605.HTM.

[19] Najmabadi, K., Evans, M. R., Coleman, E. E., Bleeg, R. J., Breuhaus, R. S., Anderson, D. M., and Nelson, T. A., "Aircraft Pitch-Axis Stability and Command Augmentation," , U.S. Patent 5 722 620, Mar. 1998. URL https://patents.google.com/patent/US5722620A/en.

[20] Field, E., "The Application of a C* Flight Control Law to Large Civil Transport Aircraft," Tech. rep., Cranfield Institute of Technology, Bedford, United Kingdom, Mar. 1993. URL https://dspace.lib.cranfield.ac.uk/handle/1826/186.

[21] Tekles, N., Chongvisal, J., Xargay, E., Choe, R., Talleur, D. A., Hovakimyan, N., and Belcastro, C. M., "Design of a Flight Envelope Protection System for NASA's Transport Class Model," *Journal of Guidance, Control, and Dynamics*, Vol. 40, No. 4, 2017, pp. 863–877. https://doi.org/10.2514/1.G001728.

[22] Lu, Z., Hong, H., Gerdts, M., and Holzapfel, F., "Flight Envelope Prediction via Optimal Control-Based Reachability Analysis," *Journal of Guidance, Control, and Dynamics*, Vol. 45, No. 1, 2022, pp. 185–195. https://doi.org/10.2514/1.G006219.

[23] Lang, J., Wang, Z., and Li, Y., "Prescribed Performance-Based Envelope Protection Control for Coaxial Compound Helicopter in High-Speed Flight," *IEEE Transactions on Aerospace and Electronic Systems*, Vol. 61, No. 5, 2025, pp. 12219–12233. https://doi.org/10.1109/TAES.2025.3571683.

[24] Yu, X., Zhou, X., Zhang, Y., Guo, L., Ye, S., and Peng, X., "Safety Control Design with Flight Envelope Protection and Reference Command Generation," *IEEE Transactions on Aerospace and Electronic Systems*, Vol. 58, No. 6, 2022, pp. 5835–5848. https://doi.org/10.1109/TAES.2022.3181109.

[25] Xie, R., He, H., Meng, X., and Fan, X., "Neural-Network-Based Dynamic Flight Envelop Protection Within Integrated Aircraft Control System," *Journal of Guidance, Control, and Dynamics*, Vol. 46, No. 6, 2023, pp. 1083–1094. https://doi.org/10.2514/1.G006872.

[26] "A319/A320/A321 Flight Deck and Systems Briefing for Pilots, STL 945.7136/97," Tech. rep., Airbus, Sep. 1998. URL https://ads-b.ca/a320/A319-320-321_Flight_Deck_and_Systems_Briefing_for_Pilots.pdf.

[27] Goupil, P., "AIRBUS State of the Art and Practices on FDI and FTC in Flight Control System," *Control Engineering Practice*, Vol. 19, No. 6, 2011, pp. 524–539. https://doi.org/10.1016/j.conengprac.2010.12.009.

[28] Sieberling, S., Chu, Q. P., and Mulder, J. A., "Robust Flight Control Using Incremental Nonlinear Dynamic Inversion and Angular Acceleration Prediction," *Journal of Guidance, Control, and Dynamics*, Vol. 33, No. 6, 2010, pp. 1732–1742. https://doi.org/10.2514/1.49978.

[29] Simplício, P., Pavel, M. D., van Kampen, E., and Chu, Q. P., "An Acceleration Measurements-Based Approach for Helicopter Nonlinear Flight Control Using Incremental Nonlinear Dynamic Inversion," *Control Engineering Practice*, Vol. 21, No. 8, 2013, pp. 1065–1077. https://doi.org/10.1016/j.conengprac.2013.03.009.

[30] Smeur, E. J. J., Chu, Q., and de Croon, G. C. H. E., "Adaptive Incremental Nonlinear Dynamic Inversion for Attitude Control of Micro Air Vehicles," *Journal of Guidance, Control, and Dynamics*, Vol. 39, No. 3, 2016, pp. 450–461. https://doi.org/10.2514/1.G001490.

[31] Beyer, Y., Steen, M., and Hecker, P., "Boosted Incremental Nonlinear Dynamic Inversion for Flexible Airplane Gust Load Alleviation," *Journal of Guidance, Control, and Dynamics*, Vol. 47, No. 7, 2024, pp. 1394–1413. https://doi.org/10.2514/1.G007984.

[32] Tal, E., and Karaman, S., "Global Incremental Flight Control for Agile Maneuvering of a Tailsitter Flying Wing," *Journal of Guidance, Control, and Dynamics*, Vol. 45, No. 12, 2022, pp. 2332–2349. https://doi.org/10.2514/1.G006645.

[33] Pfeifle, O., and Fichter, W., "Cascaded Incremental Nonlinear Dynamic Inversion for Three-Dimensional Spline-Tracking with Wind Compensation," *Journal of Guidance, Control, and Dynamics*, Vol. 44, No. 8, 2021, pp. 1559–1571. https://doi.org/10.2514/1.G005785.

[34] Liu, S., Lyu, W., Zhang, Q., Yang, C., and Whidborne, J. F., "Neural-Network-Based Incremental Backstepping Sliding Mode Control for Flying-Wing Aircraft," *Journal of Guidance, Control, and Dynamics*, Vol. 48, No. 3, 2025, pp. 600–614. https://doi.org/10.2514/1.G008215.

[35] Wang, X., van Kampen, E., Chu, Q., and Lu, P., "Incremental Sliding-Mode Fault-Tolerant Flight Control," *Journal of Guidance, Control, and Dynamics*, Vol. 42, No. 2, 2019, pp. 244–259. https://doi.org/10.2514/1.G003497.

[36] Chang, J., Breuker, R. D., and Wang, X., "Active Fault-Tolerant Incremental Sliding-Mode Flight Control Against Control Reversal," *Journal of Guidance, Control, and Dynamics*, Vol. 45, No. 12, 2022, pp. 2411–2420. https://doi.org/10.2514/1.G006690.

[37] Wang, X., and Sun, S., "Incremental Fault-Tolerant Control for a Hybrid Quad-plane UAV Subjected to a Complete Rotor Loss," *Aerospace Science and Technology*, Vol. 125, Jun. 2022, Paper 107105. https://doi.org/10.1016/j.ast.2021.107105.

[38] Atmaca, D., and van Kampen, E., "Active Incremental Nonlinear Dynamic Inversion for Simultaneous Sensor and Actuator Fault-Tolerant Control," *AIAA SciTech Forum*, Jan. 2026.

[39] Sun, D., and Hovakimyan, N., "Potential-Function-Based Command Limiting for Longitudinal Motion of Unmanned Aerial Vehicles," *Journal of Guidance, Control, and Dynamics*, Vol. 48, No. 9, 2025, pp. 2128–2137. https://doi.org/10.2514/1.G008702.

[40] Sun, D., Jafarnejadsani, H., and Hovakimyan, N., "Command Limiting for Aerial Vehicles with Rate Control Augmentation Systems," *IEEE Transactions on Aerospace and Electronic Systems*, Vol. 57, No. 3, 2021, pp. 1702–1712. https://doi.org/10.1109/TAES.2021.3050674.

[41] Sun, D., Hovakimyan, N., and Jafarnejadsani, H., "Design of Command Limiting Control Law Using Exponential Potential Functions," *Journal of Guidance, Control, and Dynamics*, Vol. 44, No. 2, 2021, pp. 441–448. https://doi.org/10.2514/1.G004972.

[42] Stroosma, O., van Paassen, M. M., and Mulder, M., "Using the SIMONA Research Simulator for Human-machine Interaction Research," *AIAA Modeling and Simulation Technologies Conference and Exhibit*, AIAA Paper 2003-5525, 2003. https://doi.org/10.2514/6.2003-5525.

[43] Park, J., Choi, J. Y., Jo, Y., and Choi, S., "Stability and Control of Tailless Aircraft Using Variable-Fidelity Aerodynamic Analysis," *Journal of Aircraft*, Vol. 54, No. 6, 2017, pp. 2148–2164. https://doi.org/10.2514/1.C034052.

[44] "Easy Access Rules for Large Aeroplanes (CS-25)," Tech. rep., European Union Aviation Safety Agency, Jun. 2022. URL https://www.easa.europa.eu/en/document-library/easy-access-rules/easy-access-rules-large-aeroplanes-cs-25.

[45] "A350-900 Flight Deck and Systems Briefing for Pilots, V00D11029337," Tech. rep., Airbus, Sep. 2011.

[46] "Type-Certificate Data Sheet for Trent XWB Series Engines, EASA.E.111," Tech. rep., European Union Aviation Safety Agency, Eschenweg, Germany, Oct. 2022. URL https://www.easa.europa.eu/en/document-library/type-certificates/engine-cs-e/easae111-rolls-royce-deutschland-trent-xwb-series.

[47] "Benchmark Requirements and Performance Metrics, 723515-INCEPTION-D2.5," Tech. rep., Cranfield University, Bedford, United Kingdom, Aug. 2018. https://doi.org/10.3030/723515.

[48] Pollack, T. S. C., "Advances in Dynamic Inversion-based Flight Control Law Design Multivariable Analysis and Synthesis of Robust and Multi-Objective Design Solutions," Ph.D. thesis, Delft University of Technology, Delft, The Netherlands, Oct. 2024. https://doi.org/10.4233/uuid:28617ba0-461d-48ef-8437-de2aa41034ea.

[49] Hanke, C. R., and Nordwall, D. R., "The Simulation of a Jumbo Jet Transport Aircraft. Volume 2: Modeling Data," Tech. rep., NASA CR 114494, Sep. 1970. URL https://ntrs.nasa.gov/citations/19730001300.

[50] Grondman, F., Looye, G., Kuchar, R. O., Chu, Q. P., and van Kampen, E., "Design and Flight Testing of Incremental Nonlinear Dynamic Inversion-based Control Laws for a Passenger Aircraft," *2018 AIAA Guidance, Navigation, and Control Conference*, AIAA Paper 2018-0385, Jan. 2018. https://doi.org/10.2514/6.2018-0385.

[51] Bacon, B., and Ostroff, A., "Reconfigurable Flight Control Using Nonlinear Dynamic Inversion with a Special Accelerometer Implementation," *AIAA Guidance, Navigation, and Control Conference and Exhibit*, AIAA Paper 2000-4565, Aug. 2000. https://doi.org/10.2514/6.2000-4565.

[52] Pollack, T. S., and Kampen, E., "Multi-objective Design and Performance Analysis of Incremental Control Allocation-based Flight Control Laws," *AIAA SciTech Forum*, AIAA Paper 2023-1249, 2023. https://doi.org/10.2514/6.2023-1249.

[53] Durham, W., Bordignon, K. A., and Beck, R., *Aircraft Control Allocation*, John Wiley & Sons, Ltd, West Sussex, United Kingdom, Nov. 2016. https://doi.org/10.1002/9781118827789.

[54] Bordignon, K., and Bessolo, J., "Control Allocation for the X-35B," *Biennial International Powered Lift Conference and Exhibit*, AIAA Paper 2002-6020, Nov. 2002. https://doi.org/10.2514/6.2002-6020.

[55] Johnson, E. N., and Calise, A. J., "Pseudo-Control Hedging: A New Method For Adaptive Control," *Advances in Navigation and Control Technology Workshop*, Nov. 2000. URL https://www.ejohnson.gatech.edu/ngct-paper-johnson.pdf.

[56] Lombaerts, T. J., Smaili, M. H., Stroosma, O., Chu, Q. P., Mulder, J. A., and Joosten, D. A., "Piloted Simulator Evaluation Results of New Fault-Tolerant Flight Control Algorithm," *Journal of Guidance, Control, and Dynamics*, Vol. 32, No. 6, 2009, pp. 1747–1765. https://doi.org/10.2514/1.44280.

[57] Lombaerts, T., and Looye, G., "Design and Flight Testing of Manual Nonlinear Flight Control Laws," *AIAA Guidance, Navigation, and Control Conference*, AIAA Paper 2011-6469, Aug. 2011. https://doi.org/10.2514/6.2011-6469.

[58] "Flying Qualities of Piloted Aircraft," Tech. rep., Department of Defense, United States, Jan. 1990.

[59] Atmaca, D., Stroosma, O., and van Kampen, E., "Design and Piloted Simulation of Envelope-Protected Control for Flying Wing Aircraft," *Journal of Guidance, Control, and Dynamics*, 2026.

[60] Cooper, G. E., and Harper, R. P., "The Use of Pilot Rating in the Evaluation of Aircraft Handling Qualities," Tech. rep., NASA TN D-5153, Apr. 1969. URL https://ntrs.nasa.gov/citations/19690013177.

[61] van Paassen, M. M., Stroosma, O., and Delatour, J., "DUECA - Data-driven Activation in Distributed Real-time Computation," *AIAA Modeling and Simulation Technologies Conference*, AIAA Paper 2000-4503, Aug. 2000. https://doi.org/10.2514/6.2000-4503.